
CHAPTER 6

Extended X-ray Absorption Fine Structure Spectroscopy

J. A. van Bokhoven¹, T. Ressler², F. M. F. de Groot³
and G. Knopp-Gericke²

¹Laboratory for Technical Chemistry, ETH Hönggerberg, CH-8093 Zurich, Switzerland

²Fritz-Haber-Institut der MPG, Department of Inorganic Chemistry, Faradayweg 4–6, 14195 Berlin, Germany

³Debye Institute, Department of Inorganic Chemistry and Catalysis, Utrecht University, Sorbonnelaan 16, 3508 TB Utrecht, The Netherlands

CONTENTS

1. Introduction	107
2. The EXAFS Function	108
2.1. Geometric Information Contained in the EXAFS Function	110
2.2. The EXAFS Equation ($\chi(k)$) in Single Scattering Approximation	110
2.3. Experimental Considerations and Detection Methods	111
2.4. Data Analysis	112
2.5. Isolation of EXAFS (I T/M IV)	112
2.6. The Fourier Transform, k^n Weighting and k -Dependency	112
2.7. Separation of Shells and Fourier Filtering	114
2.8. Fitting of Experimental EXAFS	115
3. Description of <i>in-situ</i> Cells for EXAFS for Catalytic Purposes	118
3.1. Type I: Treatment Chamber Cells	118
3.2. Type II: True Reactor Cell	120
4. <i>In-situ</i> EXAFS for Catalytic Applications	120
4.1. Catalytic Partial Oxidation	120
4.2. Structure and Nature of Active Sites in Hydrotreating Catalysts	122
5. Conclusions and Outlook	126
Acknowledgment	127
References	127

1. INTRODUCTION

XAFS spectroscopy probes the local structure of an atom, regardless of the state of aggregation of the sample. Both the

geometry and the electronic properties are explored [1, 2]. A large advantage of this technique compared to other characterization techniques that provide similar information is that it can be applied under non-ambient conditions: In catalysis research, a catalyst can be investigated under reaction conditions, thus providing information about a working catalyst.

Email: j.a.vanbokhoven@tech.chem.ethz.ch

Moreover, (pre-cursor) catalysts can be studied under synthesis and pretreatment conditions, providing insight into the processes that take place during catalyst activation. Moreover, no long-range order is necessary for performing a measurement; the materials can be amorphous solids, liquids or gasses. This explains why so many XAFS studies are devoted to catalysts [3]. Time-resolved techniques are especially useful when parameters such as temperature, pressure and gas mixture are varied and the response of the system is investigated. Moreover, development of a catalytic system such as deactivation can also be assessed with time-resolved techniques [4].

This paper deals with *in-situ* EXAFS measurements for catalytic purposes. The content has been restricted to heterogeneous catalysis, and homogeneous and bio-catalysis are omitted. An *in-situ* measurement is thus defined as an experiment carried out under non-ambient conditions, i.e., at high temperature in the presence of a gas. These may be actual reaction conditions, or the consecutive steps during the synthesis and activation of the catalyst. Other heterogeneous systems, like solid-liquid systems are excluded from the text.

In-situ measurements on elements heavier than potassium, (rather arbitrarily) the fourth row in the periodic table, are standard (within the limits of an experimental set-up). The unwanted absorption of radiation by the elements (and the air) is very significant for lighter elements (with edges of energy < 2.5 keV). The transmission of an X-ray beam through 20 cm of air is significantly suppressed at energy lower than 2.5 keV (Figure 1), thus complicating the application of *in-situ* measurements. At these edges, special care must be taken when designing and constructing *in-situ* cells, discussed elsewhere [5]. Many *in-situ* set-ups for hard X-rays have been described throughout the literature, and a selection is presented here. Furthermore, several selected examples of *in-situ* EXAFS measurements of catalytic systems are given, preceded by a concise introduction of XAS [6]: i) derivation of the EXAFS equation, ii) experimental set-up for measuring an EXAFS spectrum, and iii) data analysis procedures. This paper should provide a basic understanding of *in-situ* EXAFS measurements and their interpretation for catalytic purposes.

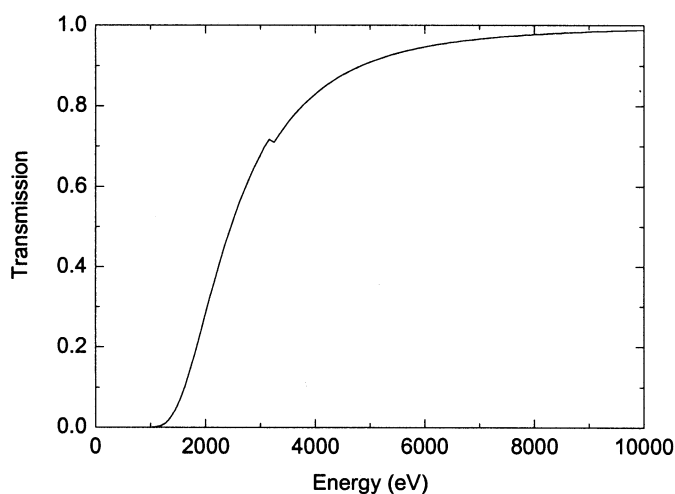


Figure 1. Calculated X-ray transmission of 20 cm air as a function of X-ray energy.

2. THE EXAFS FUNCTION

X-ray photons, traveling through a medium that is not vacuum, may be absorbed by this medium. Accordingly, a monochromatic X-ray beam, with energy $E = hv$, passing through a medium is attenuated according to Lambert Beer's law:

$$dI = -\mu(E)I dx \quad (1a)$$

$$I = I_0 \exp(-\mu(E)x) \quad (1b)$$

dI : the decrease in intensity of an X-ray beam through the path length dx

$\mu(E)$: the linear absorption coefficient specific for the medium

I : the intensity of the attenuated beam

I_0 : the intensity of the initial X-ray beam

x : the path length through the medium.

The absorption, $\mu(E)$, decays exponentially with energy. Figure 2 shows the calculated absorption as a function of energy through a platinum foil, 100 μm thick. At a certain energy (hv) when the energy of the incident beam matches or is greater than the binding energy (E_0) of a bound electron, this electron is emitted by the photo-electric effect described by Einstein. A core-hole (o) is left on the absorbing atom, and a photo-electron having kinetic energy is created (Figure 3). Due to this absorption process, the X-ray absorption through a medium as a function of energy shows a sharp increase in absorption at energy E_0 , referred to as the absorption edge. Figure 2 reveals the three consecutive L edges of the platinum foil. The binding energy (E_0) is characteristic for a bound electron in a particular atom, making the XAS experiment element-specific. All possible absorption edges have been tabulated [7].

At energies of the incident X-ray beam higher than E_0 , the kinetic energy of the photo-electron is:

$$E_{\text{kin}} = hv - E_0. \quad (2)$$

This photo-electron can be regarded as a spherical electronic wave, and the kinetic energy (E_{kin}) of the photo-

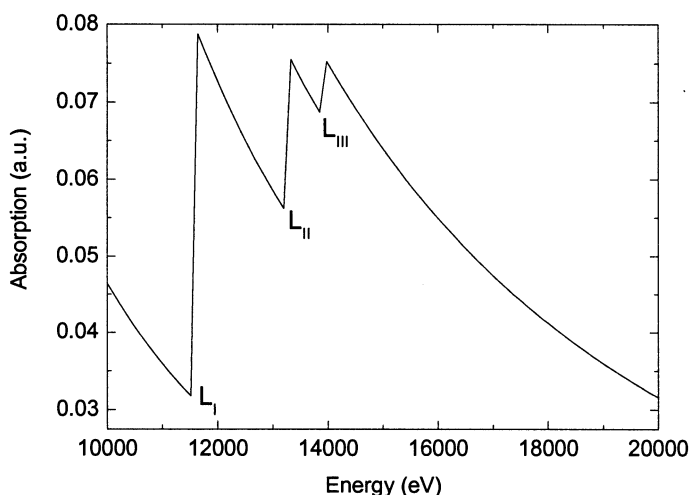


Figure 2. The three consecutive L edges of Pt calculated for a Pt foil.

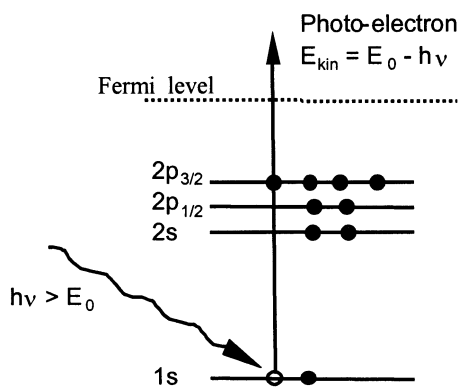


Figure 3. In an XAS experiment, a core-electron is excited by absorption of a photon. A photo-electron is created having kinetic energy, leaving a core-hole on the absorbing atom.

electron determines the wavelength (λ), defined as $\lambda = 2\pi/k$; k is the so-called photo-electron wave vector having an energy proportional to the square root of the kinetic energy:

$$k = \left[\left(\frac{8\pi^2 m}{h^2} \right) (h\nu - E_0) \right]^{1/2} \quad (3)$$

m : the electron mass

h : Planck's constant.

This electronic wave expands concentrically from the absorbing atom **A** (solid circles in Figure 4) and is referred to as the *outgoing wave*. It may be scattered while 'hitting' a potential well or potential gradient, induced by the presence of electrons on neighboring atoms, producing the so-called *backscattered wave* (broken circles in Figure 4). These two waves form an interference pattern, with constructive interference where they have the same sign and destructive interference where they have an opposite sign. Thus, *the final state* consists of two interfering waves, the outgoing and the backscattered wave (Figure 4):

$$\Psi_{Final} = \Psi_{Outgoing} + \Psi_{Backscattered} \quad (4)$$

Expressing the absorption process in the dipole approximation, the probability of photo-electric absorption (P) being proportional to the X-ray absorption coefficient ($\mu(E)$) is given by Fermi's Golden Rule:

$$\mu \propto P = \frac{2\pi^2 e^2}{\omega c^2 m} \left| \langle \Psi_{final} | \mathbf{E} \cdot \mathbf{r} | \Psi_{initial} \rangle \right|^2 \rho(E_f) \quad (5)$$

ω : the angular frequency

e : the electron charge

Ψ_{final} : the final state wave function (equation 4)

$\Psi_{initial}$: the initial (ground state) wave function of the bound electron

\mathbf{E} : the electric field polarization vector

\mathbf{r} : the position vector of the scatterer with respect to the absorber atom

$\rho(E_f)$: the density of allowed states at the final energy E_f .

The electric field polarization vector \mathbf{E} and position vector \mathbf{r} determine whether the transition is (dipole) allowed or not.

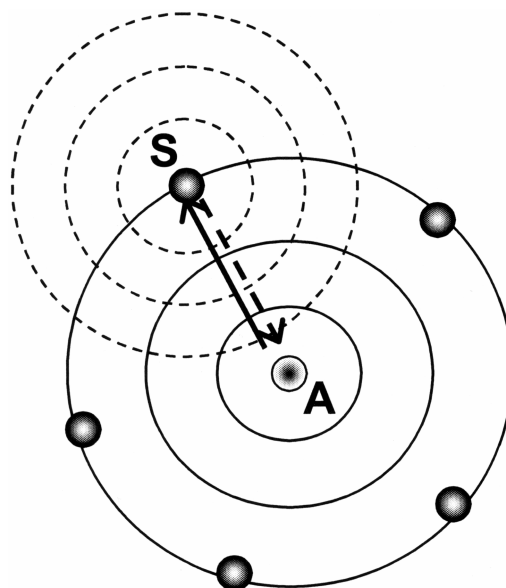


Figure 4. A photo-electron, represented as an expanding wave (solid circles) from the absorber atom **A**, is scattered by the neighboring atoms, **S**. Schematically, the backscattered wave against one of the neighboring atoms is illustrated (dashed circles).

Since the final state (Ψ_{final}) is a function of two interfering contributions (equation 4) that are both a function of energy of incident beam, the transition probability (P) is not a smooth function of energy above the absorption edge. The absorption shows the respective minima and maxima that constitute the EXAFS signal[#]. Figure 5 depicts an XAS spectrum of a copper foil taken at the Cu K edge. The abscissa represents the absolute energy of the X-rays, and the ordinate

[#]The respective maxima and minima make the absorption 'wiggle', hence the term EXAFS-wiggles.

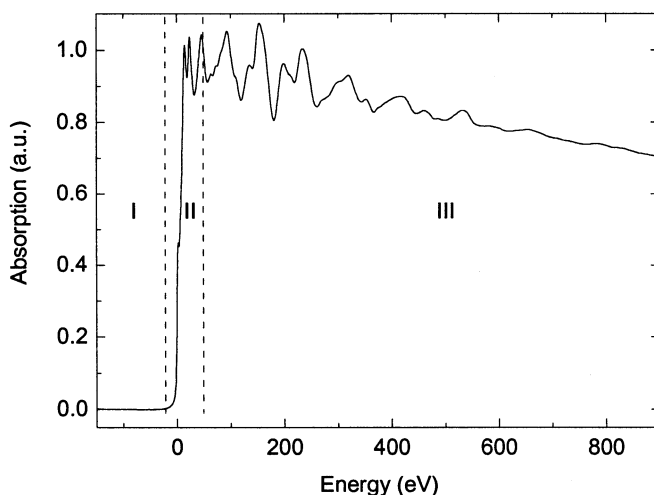


Figure 5. Cu K edge XAS spectrum of a copper foil with three distinct regions of a spectrum.

shows the (normalized) absorption coefficient. A spectrum is divided into three regions:

- (i) The smooth exponentially decaying region before the edge. Features may be visible several eV below the absorption edge.
- (ii) The XANES (X-ray Absorption Near edge Structure) region, starting with the so-called absorption edge. This region of the spectrum is discussed elsewhere [8].
- (iii) The Extended X-ray Absorption Fine-Structure (EXAFS) region, starting at ~ 50 eV above the absorption edge.

The oscillatory part (iii) of the absorption coefficient is the EXAFS function ($\chi(k)$) with:

$$\mu(k) = \mu_0(k)\{1 + \chi(k)\} \quad (6)$$

and μ_0 is the atomic background, representing the X-ray absorption of a free atom.

2.1. Geometric Information Contained in the EXAFS Function

It is shown above that, at $h\nu \geq E_0$, the transition probability of an X-ray beam through a medium is a variable “wiggling” function of energy. Geometric information is provided by the absorption spectra. This can be understood phenomenologically, if the scattering process is observed. The absorption process is a function of interference of the two contributions constituting the final wave, the outgoing and the backscattered wave (equations 4 and 5, Figure 4). The backscattering occurs against potential wells (or gradients) at neighboring atoms. Atoms at different positions induce a different interference pattern and, thus, distinguishable absorption spectra. This too accounts for the kind (Z) and number (N) of neighboring atoms, and their disorder (σ) (both static and thermal): Different neighboring atoms will scatter the wave differently, determining both the phase and the amplitude of the scattered wave. These variables are all mathematically represented in the EXAFS equation ($\chi(k)$). To obtain this geometric information, the $\chi(k)$ function is analyzed in detail, as discussed below.

In short, an XAS experiment gives structural information, because the interference pattern of the outgoing and backscattered wave of the photo-electron and, thus, the transition probability (equations 4 and 5), is a variable function of the energy of the incident X-ray beam. The interference pattern is a function of the scattering by the neighboring atoms and, thus, of the position, number and kind of neighboring atoms. An EXAFS spectrum, therefore, gives information about the local structure around the absorber atom. Neighboring atoms are divided into so-called coordination shells, containing N atoms of the same element at (about) the same distance.

2.2. The EXAFS Equation ($\chi(k)$) in Single Scattering Approximation

Assuming that the photo-electron scatters only once during its lifetime (the so-called single scattering approximation,

valid at approximately 50 eV above the absorption edge), the EXAFS function ($\chi(k)$) can be described as:

$$\chi(k) = \sum_{j=1}^j A_j(k) \sin(2kR_j + \phi_j(k)) \quad (7)$$

with j referring to the j th coordination shell

R_j : the distance between the absorber atom and the atoms in the j th shell

$A_j(k)$: the backscattering amplitude

$\phi_j(k)$: the phase-shift experienced by the photo-electron in the scattering process.

There are excellent reviews in the literature giving a detailed derivation of this equation. Both $A_j(k)$ and $\phi_j(k)$ are complex functions of wave vector k (equation 3). The phase-shift ($\phi_j(k)$) is a complex function, unique for each pair of absorber and scatterer atoms and a non-linear (decreasing) function of k . The backscattering amplitude ($A_j(k)$) is expressed as a product of three terms:

$$A_j(k) = \frac{S_0^2 e^{-2R_j/\lambda}}{kR_j^2} \times e^{-2\xi_j^2 k^2} \times N_j F_j(k) \quad (8)$$

The first term represents *damping* of the signal, the second the *disorder* in the material under investigation and the latter the *scattering power* of shell j .

In the damping term, S_0^2 is the so-called amplitude reduction factor and approximates the loss of intensity due to the loss of photo-electron energy: The energy transfer between the photon and the photo-electron is incomplete due to many body effects and shake-up/shake-off processes in the absorber atom. The size of S_0^2 is usually between 0.75 and 0.95 [9]. The mean free path, (also) λ in the exponential term $e^{-2R_j/\lambda}$, is a function of the energy of the photo-electron as determined by the lifetime of the final state. The term $1/R_j^2$ accounts for the loss of intensity due to the spherical character of the wave of the photo-electron. The second term describes the disorder and includes the Debye-Waller factor, σ_j^2 . It represents the fluctuation in R_j by thermal motion and the structural disorder in the material, defining thermal and static disorder, respectively. The scattering power (the third term) is determined by the number (N_j) of neighboring atoms in the j th shell and the scattering power of neighbor j ($F_j(k)$). It is a strong function of wave vector k and, moreover, unique for each atom.

All the terms in equation 8 have a different dependency on k , facilitating differentiation between these terms when analyzing experimental data. Effectively, the scattering of the photo-electron (Figure 4) occurs off electrons on neighboring atoms with an orbital energy E_{orb} . Most efficient scattering occurs off electron density with about the same orbital energy as the kinetic energy of the photo-electron. Therefore, a light-neighboring atom will scatter the outgoing electrons with a relatively low kinetic energy, while the heavier atoms scatter the photo-electron more effectively when it has a high kinetic energy (up to ~ 500 eV above the absorption edge). The next-nearest neighboring atoms in the periodic table show sufficient difference in $F_j(k)$ (and $\phi_j(k)$!) to distinguish between

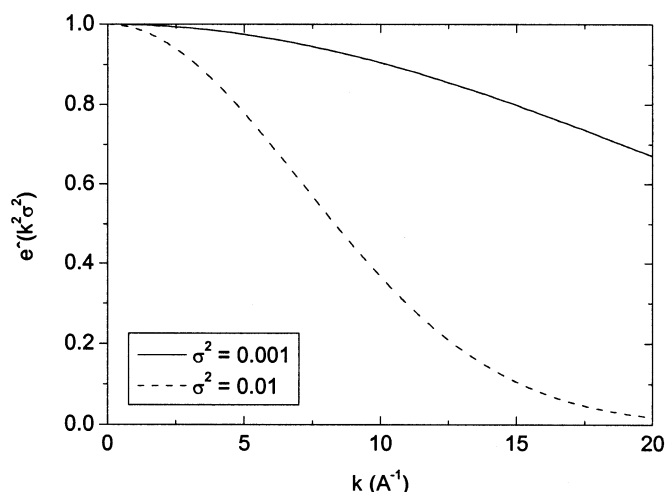


Figure 6. The exponential decay of the Debye-Waller term in the backscattering function for two experimental encountered values of σ_j^2 .

these atoms as scatterer atoms. In the data analysis section, this difference in scattering is used to distinguish light and heavy scatterers.

The Debye-Waller factor (σ_j^2) decays with k via $e^{-\sigma_j^2 k^2}$ (Figure 6). Two values of σ_j^2 which may be experimentally encountered are indicated. For absorption-backscatterer pairs having a large Debye-Waller factor (dashed line) due to high structural disorder or due to measurement at high temperature (thermal disorder), the EXAFS signal decays very rapidly with k .

2.3. Experimental Considerations and Detection Methods

Experimental spectra are obtained by measuring the absorption of X-rays of a sample (equation 1). In the hard X-ray regime, spectra are usually measured in the transmission mode, directly measuring the attenuation of the intensity of the X-ray beam. The intensity of an X-ray beam before (I_0) and after (I_T) a sample is measured, usually with ionization chambers or photo diodes (Figure 7), defining the absorption coefficient by:

$$\mu(k) \cdot x = -\ln\left(\frac{I_T}{I_0}\right) \quad (9)$$

However, if the element under study is very diluted in the sample or if the sample cannot be made thin enough to allow sufficient radiation to pass through the sample without being (almost) completely absorbed, other detection methods are required. The process of exciting an electron from a core level creates a core-hole (Figure 3); thus, any detection method that measures a signal that is proportional to the number of core-holes is also proportional to the absorption coefficient. In practice, the annihilation of the core-hole is used to measure an XAS spectrum with either fluorescence or electron yield detection. Figure 8 indicates these two annihilation processes, the radiative (left side) and the non-radiative (right side) electronic transition from a lower binding energy level. Radiative transmissions produce fluorescence radiation of

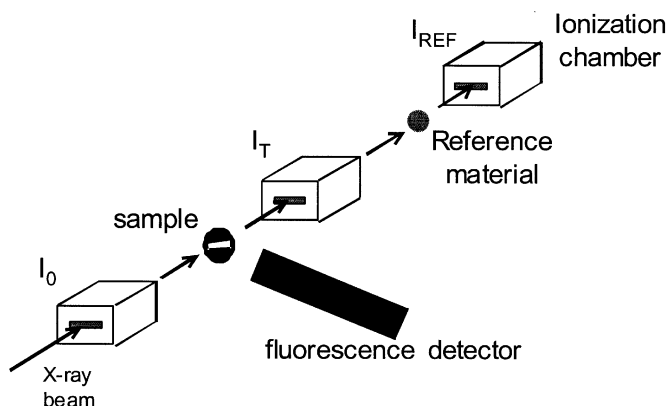


Figure 7. Experimental set-up for performing an EXAFS experiment.

typical energy; Auger electrons are produced in the non-radiative process. This process is followed by a cascade of decays, leading to a flux of low-energy electrons. The lower the energy of the absorption edge, the higher the probability of Auger decay [10].

Auger detection is surface-sensitive because of the small escape depth of the low-energy electrons compared to photons. This escape depth can be significantly less than ~ 50 Å for metals and semiconductors in the 50 to 150 eV spectral range. In insulators, less likely electron-electron scattering increases this value somewhat [5, 11]. Total electron yield (TEY) is the usual method, measuring all the electrons coming from the sample. This signal is dominated by the inelastically scattered Auger electrons that are proportional to the EXAFS. However, other methods are used [12] that provide further surface-enhanced sensitivity.

In the case of fluorescence detection, an energy-dispersive detector is often used that selects the photons that are proportional to the X-ray absorption process. However, in the case of a heavy atom in a light matrix, total fluorescence yield is used with success. The sample is placed at an angle of 45 degrees to the incoming X-rays, and the detector at an angle of 90 degrees. Decreasing the incoming angle of the X-rays on the sample decreases the penetration depth, enhancing the surface sensitivity and eventually enabling the investigation of the outermost layer(s) of a substrate [12].

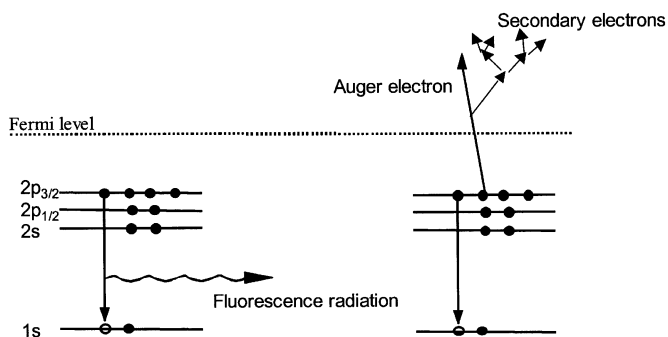


Figure 8. Annihilation processes of the core-hole. The radiative decay (fluorescence yield) is given on the left, the non radiative decay (electron yield) is given on the right.

With electron yield and fluorescence yield detection, the absorption coefficient is given by:

$$\mu(k) \propto \frac{I_S}{I_0} \quad (10)$$

I_S : the electron yield or fluorescence yield signal

I_0 : the intensity of the incoming X-ray beam.

The amount of sample that an X-ray beam must traverse (the path length x) determines the amount of absorption. A sample that is too thick absorbs the X-ray beam almost completely. Moreover, the edge step of the element under investigation must be large enough to enable isolation of the EXAFS signal. A very small edge step will show a very low S/N level in the EXAFS signal, although the noise in the measured incident and transmitted beam may be low. In general, an ideal edge step of the element under study is $\Delta\mu(E) = 1$ and the maximum absorption must not exceed a value of $\mu(E)x = 2.55$ for the best signal-to-noise ratios. These values can be calculated using tabulated absorption coefficient values [13].

2.4. Data Analysis

After obtaining XAS spectra, the information about the local structure around the absorber atom must be extracted from the EXAFS data. Many different (commercial) data analysis programs exist [14]; XDAP [15] is used here. The scheme of data analysis consists of the following consecutive steps, which are elaborated below [6]:

- (i) subtraction of the monotonically decreasing background
- (ii) determination of the edge position, E_0
- (iii) determination of the atomic background
- (iv) subtraction of the atomic background and normalization on an atomic basis
- (v) fitting of the EXAFS data using references.

2.5. Isolation of EXAFS (I T/M IV)

Equation (6) defines the EXAFS function, $\chi(k)$ which must be fitted:

$$\chi(k) = \frac{\mu - \mu_0}{\mu_0} \quad (11)$$

A first step in the data analysis is the subtraction of the monotonically decreasing pre-edge. A function is fitted to the pre-edge region and extrapolated over the whole data range (Figure 9a). Here, a modified Victoreen [2] is used, but sometimes other or more complicated functions are used. After subtracting the data with the fitted pre-edge function, the edge energy position must be determined. The edge position is E_0 in equation 3 and, thus, the zero point of k (\AA^{-1}). Therefore, the choice of the zero point, or rather the inner potential, influences the fitting parameters (vide infra); thus, care should be taken. Several methods are used to determine the edge position. A general definition of the edge position is the inflection point in the edge, easily determined through the

maximum in the first derivative, as shown in Figure 9b. However, sometimes, the edge contains fine structure due to the presence of resonances and/or electronic excitations, making it difficult to assign the inflection point. To avoid miscellaneous arbitrary choices of the edge position, the energy at half height of the total edge step is often taken as (an arbitrary choice of) the edge.

Once the edge position has been determined, the atomic background (μ_0) should be determined and subtracted from the data (equation 11, Figure 9c). A cubic spline is used here, but other functions can also be used. This choice was made, based on the subtle variations in μ_0 that can be obtained when this function is used:

$$\sum_{i=1}^{NPTS} \frac{(\mu x_i - BCK_i)^2}{e^{-Wek_i^2}} \leq Sm \quad (12)$$

Sm: Smoothing parameter

We: Weighting factor

i : NPTS defines the start and end energy of the background.

Four parameters can be varied using the cubic spline function: Sm, We, E_{start} and E_{end} . E_{start} and E_{end} define the limits of i . Larger values of Sm give a background that is less smooth, eventually approaching a straight line. The goal is to find the optimum background, so that no oscillatory signals of $\chi(k)$ are subtracted from the data and that only true XAFS signals are present in the remaining signal. It was found recently that the so-called *Atomic* XAFS (AXAFS) contains valuable information [16]. To separate the AXAFS from the smooth background and from double-electron excitations, a very precise evaluation of the background must be performed, as described recently [17], although other approaches have also been reported [18].

After subtracting the background and before the fitting, the data must be normalized on a per atom basis, which is done by dividing the data by the edge step above the absorption edge. The magnitude of the background at 50 eV is used here, but other values or division by the atomic background will give very similar results (Figure 9c). Once the above-mentioned steps have been taken, the $\chi(k)$ data are isolated (Figure 9d) and can be fitted in order to extract the valuable structural information.

2.6. The Fourier Transform, k^n Weighting and k -Dependency

The insight that Fourier transformation of the EXAFS function represents the atomic radial distribution function around the absorber atom [19] has been a major breakthrough for obtaining structural information from EXAFS data. The Fourier transform is defined by:

$$FT(r) = \frac{1}{2\pi} \int_{k_{\min}}^{k_{\max}} k^n \cdot \chi(k) \cdot e^{2ikr} dk \quad (13)$$

Application of this function shows the EXAFS data of the copper foil in R space (Figure 10). The magnitude of the

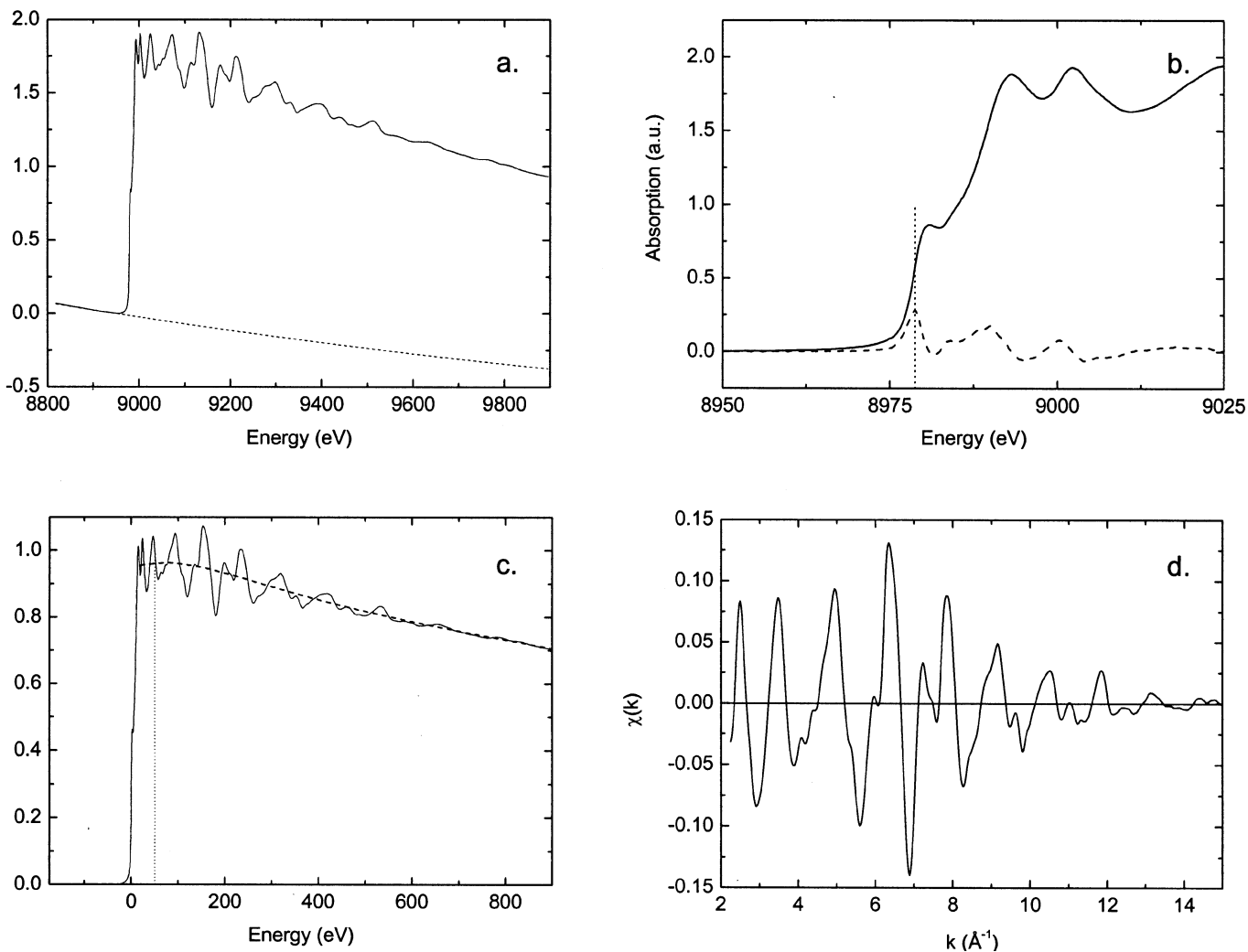


Figure 9. EXAFS data analysis scheme of Cu foil at the Cu K edge spectrum. a) Subtraction of pre edge; b) Absorption edge determination; c) Subtraction of background and normalization; d) Produced EXAFS data.

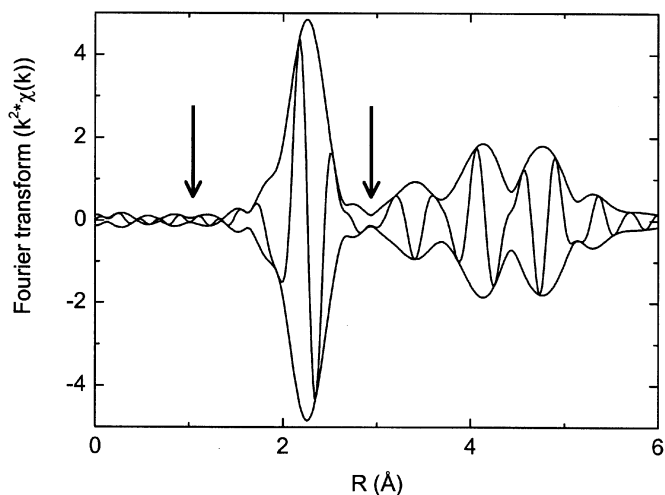


Figure 10. k^2 -weighted Fourier transform of EXAFS of Cu foil; $3.3 < k < 14.9$.

Fourier transform contains both the real (Re) and imaginary part (Im) according to:

$$|FT| = \sqrt{\text{Re}^2 + \text{Im}^2} \tag{14}$$

Figure 10 shows the magnitude of the Fourier transform (solid line) and the imaginary part (dashed line). The magnitude of the Fourier transform depends on the backscattering amplitude (equation 7) and, therefore, on the number of neighboring atoms in combination with the Debye-Waller factor. The imaginary part is very sensitive to the bond length of the absorber-scatterer pair in combination with the phase-shift experienced by the photo-electron during the scatterings process.

When performing a Fourier transform some variables can be adjusted; these include k_{\min} , k_{\max} and k^n . Both k_{\min} and k_{\max} define the data range that is transformed, whereas k^n determines the so-called k -weighting that is applied: the data points are multiplied by the corresponding k value to the order of n . In principle, k^0 , k^1 , k^2 and k^3 weightings are used in

the literature, although higher weightings have occasionally been reported. In general, a weighting higher than $n = 3$ (“ k -cube-weighting”) does not provide useful data, because amplification of the (unfortunately omni-present) noise will obscure the spectra. The shape of the Fourier transform of a specific EXAFS signal is a function of these four variables. Thus, when a Fourier transform is presented, these values should be added to enable the correct interpretation of the structural data in a Fourier transform.

In general, the EXAFS function is plotted with a k weighting, so the corresponding $k^n \chi(k)$ function shows equal intensity over the whole k range. A Fourier transform of such a function shows the highest resolution, which is often obtained with the highest k weightings. However, care has to be taken when the suspicion exists that an experimental EXAFS function may include both heavy and light scatterers. Figure 11 represents the backscattering power ($F_j(k)$) of Pt-Pt and Pt-O backscatterer pairs. The heavy scatterer has a dominant contribution at high k values, whereas the light scatterer contributes very little at k values above $\sim 10 \text{ \AA}^{-1}$. The effect of a k^3 weighting is shown in the figure at the right. It is clear from the figure that the contribution of the oxygen atom is virtually negligible compared to the Pt atom. All the other terms in equations 7 and 8 are assumed to be equal for these two elements, which is a good approximation for the discussion. Integration of the area below the Fourier transforms for the often-applied experimental k ranges ($3 < k < 15$) highlights the difference between the contribution of the heavy scatterer and the lighter scatterer. Without k weighting, the area below the backscattering amplitude of Pt-Pt is 1.5 times bigger than the area below that of Pt-O. In a k^3 weighting, the area of the Pt-Pt contribution is 5 times bigger. Including higher k values magnifies the effect. Thus, in the case of a small metal particle with an average metal-metal coordination number of $3 > N > 8$ on an oxidic support giving, on average, few metal oxygen bonds ($N < 2$), applying low k weightings is vital for the determination of the metal oxide contribution [20, 21]. This example is representative of all cases in which both heavy and light scatterer atoms are present. Moreover, a heavy scatterer that has a large Debye-Waller factor will also

show little intensity at high values of k (Figure 6). Although often effective, application of k^3 weighting *by default* is precarious and therefore ill-advised [22]. In paragraph 2.8.5, an example is given.

A Fourier transform represents a radial distribution function around the absorber atom, in this case a Cu atom in copper foil (Figure 10). The figure reveals that the maximum of the magnitude of the first peak in the Fourier transform peaks at around 2.2 \AA , whereas the true Cu-Cu distance in Cu metal is 2.56 \AA . This is because the argument of the sine function in the EXAFS function (equation 7) is:

$$\text{Argument} = [2kR_j - \varphi_j(k)] \quad (15)$$

and φ_j is a non-linear function of wave factor k . This term shifts the peaks in a Fourier transform to lower R , viz. ~ 0.2 and 0.5 \AA for heavy and light scatterer atoms, respectively. The peak corresponding to a single shell in the Fourier transform is not always symmetric, but may have several shoulders. This also originates from the non-linear phase-shift and backscattering amplitude functions of k . These shoulders are easily misinterpreted as being signatures of overlapping shells.

2.7. Separation of Shells and Fourier Filtering

In k space, contributions of different shells wiggle and overlap over the whole k range. In the Fourier transform, these contributions may be isolated if the inter-atomic distances (R) are sufficiently different. Only then (as in Figure 10) can Fourier filtering be applied and a reverse Fourier transformation to the k space of this filtered contribution be made (the filtered ranges are given with arrows at $R = 1.0$ and 2.9 \AA). Figure 12a shows the filtered shell (dashed line) with the original EXAFS data plotted over it (solid line). This filtered shell can now be fitted, however, and fitting directly in R space (without Fourier back transformation) has its benefits (vide infra). A new Fourier filtering of the dashed line gives the Fourier transform of the filtered shell in Figure 12b, showing overlapping peaks, but without the higher shells. During a back transformation, errors in Fourier filtering occur, and the reliable range in k space decreases with $\Delta k \sim$

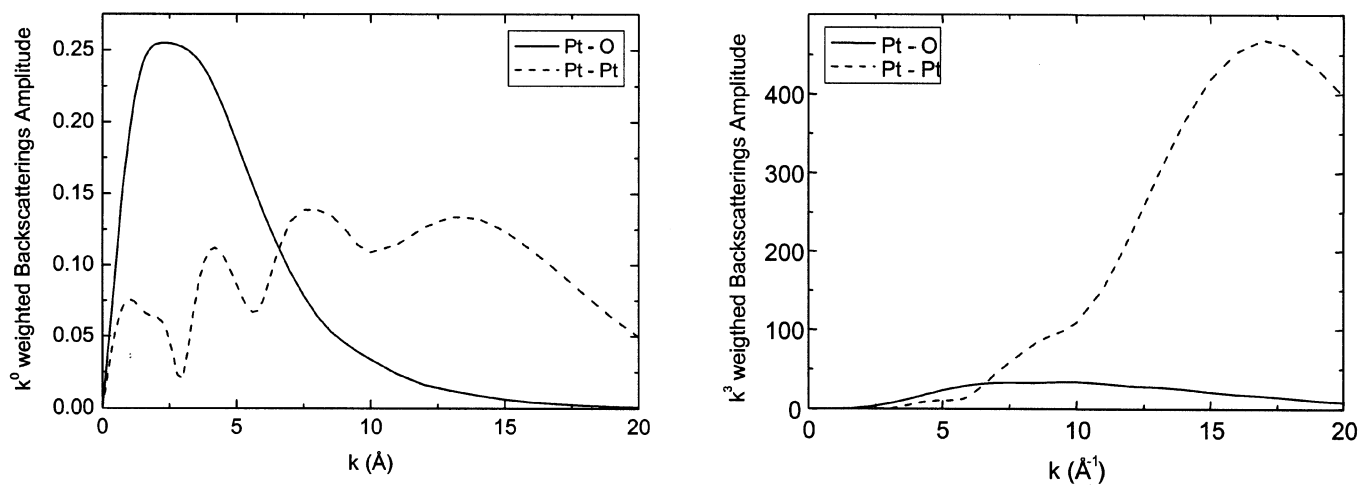


Figure 11. Backscatterings amplitude of Pt-O (solid lines) and Pt-Pt (dashed lines) scatterer pairs after k^0 (left)- and k^3 (right) weighting, illustrating the relative contribution of the light (oxygen) and the heavy (platinum) scatterer as function of k -weighting.

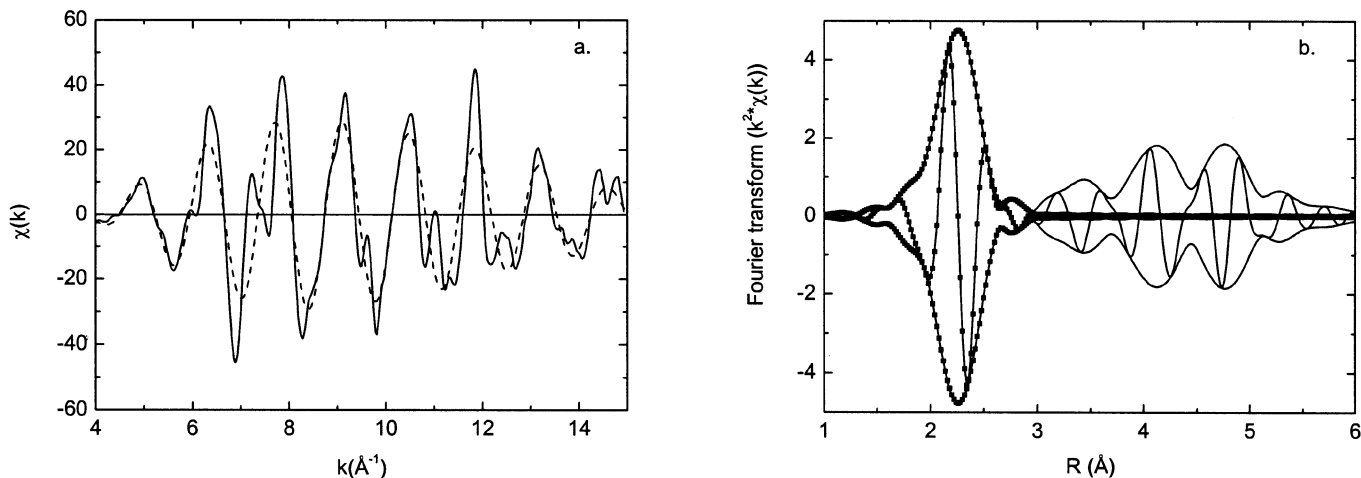


Figure 12. a. The filtered Cu-Cu first shell ($1.0 < R < 2.9$, dotted line) overplotted with the original EXAFS data (solid line), containing structure of all scattering shells. b. Corresponding Fourier transforms of the EXAFS data in a. Original EXAFS data (solid line) and filtered first Cu-Cu shell (squares), k^2 weighted, $3.2 < k < 14.9$.

$0.5\text{--}1 \text{ \AA}^{-1}$ at both extremes of the data range [23]. This decreases the amount of reliable data range and, consequently, the amount of information that can be obtained from the experimental data (loss of independent parameters, *vide infra*).

2.8. Fitting of Experimental EXAFS

2.8.1. Making References

The useful information in the EXAFS function $\chi(k)$, viz. the coordination number, distance and disorder, must be extracted from the data. Since the $\chi(k)$ function (equation 7 and 8) contains a rather high number of additional unknown parameters, such as $F_j(k)$, $\varphi(k)$, S_0^2 and $e^{-2R/\lambda}$, it is not clear how the desired information can be extracted. The general assumption is that these unknown parameters can either be calculated or determined from a spectrum of a well-known compound with an identical absorber backscatterer pair. In the case of a reference compound, the EXAFS spectrum is measured and the $\chi(k)$ function of a certain absorber backscatterer pair is isolated by means of Fourier filtering, as described above. The coordination number (N_j) and distance (R_j) are precisely known, for example, from X-ray diffraction. Therefore, in the isolated experimental $\chi_{\text{REF}}(k)$ function:

$$\chi_{\text{REF}}(k) = A_{\text{REF}}(k) \sin(2kR_{\text{REF}} + \varphi_{\text{REF}}(k)) \quad (16)$$

$$A_{\text{REF}}(k) = \frac{S_0^2 e^{-2R_{\text{REF}}/\lambda}}{kR_{\text{REF}}^2} \times e^{-2\xi_{\text{REF}}^2 k^2} \times N_{\text{REF}} F_{\text{REF}}(k) \quad (17)$$

the backscattering amplitude ($F_{\text{REF}}(k)$), phase-shift ($\varphi_{\text{REF}}(k)$), S_0^2 and λ are the unknown parameters of the concerning absorber backscatterer pair. Assuming that these factors and terms can be transferred from one compound to the other (with identical absorber backscatterer pairs), the local structure of an unknown compound can be assessed [24]. This method works well if the $\chi_{\text{REF}}(k)$ function in the reference compound is separated from other contributions in the

Fourier transform, thus limiting the choice of reference material. When a suitable reference compound is not available for a specific scatterer, a reference compound containing the neighboring atom in the periodic table is sometimes used. For example, instead of an oxygen neighbor, a nitrogen atom is sometimes used in the reference compound. This is valid, because the oxygen atom contains one extra valence electron, which has a limited effect on the scattering of the photoelectron. The reliability range of the obtained backscattering amplitude (including S_0^2 and λ) and phase-shift is, in a good case, $3 < k < 15$. As mentioned above, the (back) transformation of the data limits the accurate data range (about $\Delta k = 0.5 - 1 \text{ \AA}^{-1}$) at the beginning and end of the total k range, as the result of truncation errors. When the data range at the high-energy end is relatively small, due to a very large disorder or an exceptional amount of noise, it is desirable to extend the reliability range of the reference file at the low end of the data range. A maximum data range is of great importance when one is particularly interested in the contributions that have significant intensity only at the lowest k values (such as the atomic XAFS or when heavy scatterers dominate the EXAFS pattern at the cost of a light scatterer (Figure 11)). Furthermore, a suitable reference compound is not always available. In all of these cases, theoretical references are very effective. Currently, programs exist to theoretically calculate the backscattering amplitude, phase-shifts, S_0^2 and λ . The FEFF-code, developed by Rehr and co-workers is frequently used. Other often-used codes are EXCURVE and GNXAS [14]. The latest version (FEFF8 [25]) is a self-consistent real-space, full multiple scattering ab-initio code that calculates the X-ray absorption spectrum and electronic structure simultaneously. The backscattering amplitude, phase-shift, S_0^2 and λ for any absorber backscatterer pair can be determined with this (or any other accurate) code. Although input parameters for the FEFF-code are kept to a minimum, care must be taken in selecting the potential and other input values, which affect the output. Input parameters, such as the potential, the Debye-Waller factor and S_0^2 should be altered until the theoretical XAFS spectrum is very similar to the experimental $\chi(k)$ spec-

trum of a reference compound (when available). Such calibration with low and high k weightings of calculated backscattering amplitude and phase-shift to a standard compound, minimizes systematic errors in the analysis. When carried out in R space, Fourier back transformation is unnecessary; thus, without making truncation errors, this theoretical reference is valid starting at $k = 2.5 \text{ \AA}^{-1}$ and can be used to fit the spectra of compounds of an unknown structure.

The use of theoretical references enables EXAFS data-analysis beyond the first coordination shell, including all calculated multiple scattering paths [4]. The short-range structure of individual phases in phase mixtures can be determined [26].

2.8.2. Fitting of Unknown Compounds

The function that is minimized to obtain the structural information from the unknown compound is:

$$\chi_{\text{exp}}(k) = \sum_{j=1}^J \frac{N_j}{k_j' R_j^2} e^{-2k_j' \Delta \xi_j^2} F'_{\text{REF}}(k_j') \times \sin[2k_j' R_j + \varphi_{j,\text{REF}}(k_j')] \quad (18)$$

$\chi_{\text{exp}}(k)$: Experimental EXAFS

$\sum_j^J \dots$: Summation of all (J) fitted contributions (j)

$\Delta \sigma_j^2$: Debye-Waller factor relative to the reference

$F'_{\text{REF}}(k')$: Backscattering amplitude of the reference, including the terms S_0^2 and $e^{-\frac{2R}{\lambda}}$.

Furthermore, k' denotes the so-called 'corrected wave factor', taking into account the difference in the inner potential (ΔE_0) compared with the reference compound:

$$k' = \sqrt{k^2 + \frac{2m_e}{\hbar} \Delta E_0} \quad (19)$$

The minimization of equation 18 is achieved by varying the N_j , R_j , $\Delta \sigma_j^2$ and ΔE_{0j} of the respective shells until the absolute minimum in the function has been reached. Local minima may be encountered, and care should be taken not to interpret these as the true minimum. The average local structure around the absorber atom is established by means of the true minimum.

The available data range determines the maximum number of independent parameters (ν) [27]:

$$\nu = \frac{2\Delta k \Delta R}{\pi} + 2 \quad (20)$$

ν : number of free parameters

Δk : total range in k space

ΔR : total range in R space.

The choice of limits in k space (k_{min} and k_{max} in equation 13) and R space (R_{min} and R_{max}) determine the number of independent parameters included in the data with statistical rigor. Limiting the ΔR range decreases the number of shells that are fitted, but also the total number of free parameters,

thus still enabling the accurate determination of the first (two) coordination shells.

2.8.3. Asymmetric Distribution Functions

The use of references for fitting an EXAFS spectrum presumes that backscatterings' amplitude and phase shift can be transferred from one spectrum to the next. In general, reference data are obtained from well-defined crystalline bulk structures. However, sometimes this may lead to errors in the fitted parameters due to the presence of anharmonic vibrations (28). Normally, Gaussian pair distributions are assumed, but in the case of, for example, well-dispersed metal particles on a support, non-Gaussian vibration may lead to a pair distribution function deviating from that of the reference material. The higher the temperature, the more dominant this effect will be, which is of high importance for *in-situ* experiments. Moreover, the presence of static anharmonic disorder with a non-Gaussian distribution of bond distance and/or coordination number will give an asymmetric pair distribution function.

The presence of asymmetric distribution functions results in a reduction of the amplitude of the EXAFS signal, which is sometimes accompanied by a contraction in bond distance. The occurrence of asymmetric distribution functions can be observed by systematic measurement of the temperature dependency and observation of coordination numbers and bond distances. However, few studies discuss the possible presence of asymmetric distribution functions. Clausen et al. [28] performed molecular dynamic simulations of small Cu and Pt particles and determined asymmetric distribution functions. A systematic decrease in coordination number is observed, and in case of small Pt particles, it coincided with a decrease in bond length.

2.8.4. Goodness of Fit

Many mathematical descriptions that provide insight into the quality of the fit exist [29]. Here, as a measure of fit quality, the variance of the k^n -weighted fit is defined for fitting in k -space (21) and R -space (22), respectively, as

$$\text{variance} = \frac{\int \left\{ \left[k^n (\chi_{\text{model}}(k) - \chi_{\text{exp}}(k)) \right]^2 dk \right\}}{\int \left\{ k^n \chi_{\text{exp}}(k) \right\}^2 dk} \times 100\% \quad (21)$$

$$\text{variance} = \frac{\int \left\{ \left[k^n (FT_{\text{model}}(R) - FT_{\text{exp}}(R)) \right]^2 dR \right\}}{\int \left\{ k^n FT_{\text{exp}}(R) \right\}^2 dR} \times 100\% \quad (22)$$

As a rule of thumb, a fit quality with a variance lower than 1% can be assumed acceptable.

2.8.5. Example of Analysis, k^n weighting and Difference File Technique

The analysis of a Cu K edge spectrum of copper-arene thiolate ($\text{Cu}_3(\text{SAR})_3$) is an example of complex data analysis because several overlapping shells are present. This substance is

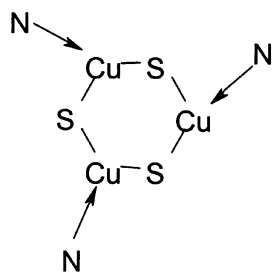


Figure 13. Trimeric structure of Copper arene-thiolate catalyst.

a selective catalyst for 1,4-Michael additions. Using Cu K edge (at 8979 eV) EXAFS spectroscopy, the structure of this catalyst before, during and after reaction is investigated to unravel the mechanistic aspects [22, 30]. Trimers of copper-arene thiolate molecules form a six-membered ring with alternating Cu and S atoms (Figure 13). Every copper atom is coordinated to two sulfur atoms and a single nitrogen atom. Carbon atoms are also present, but are further away. Various authors discussed the analysis of Cu K edge spectra of these and similar organometallic compounds and reported difficulty in detecting the Cu-Cu contribution [31].

The Fourier transform of the raw EXAFS data in k^0 - and k^3 weighting (Figure 14, left and right axis, respectively) are very different, especially in the imaginary part. This originates from the different k -dependency of all of the contributions in the EXAFS. Table 1 gives the structure of the complex based on X-ray crystallography, in addition to the final fitted EXAFS values. The first four coordination shells show excellent agreement with the crystallographic data, certainly within the error margins of both measurement techniques. The distance of Cu-C^b is too long, probably because several partially overlapping contributions are present at longer distances. The following fitting procedure was followed during the analysis of this spectrum. First, a two-shell fit was made of the first two coordination shells. Step by step, all of the higher shells were included in the fit and, in each case, all of the parameters were consecutively set free and optimized. The criterion for consid-

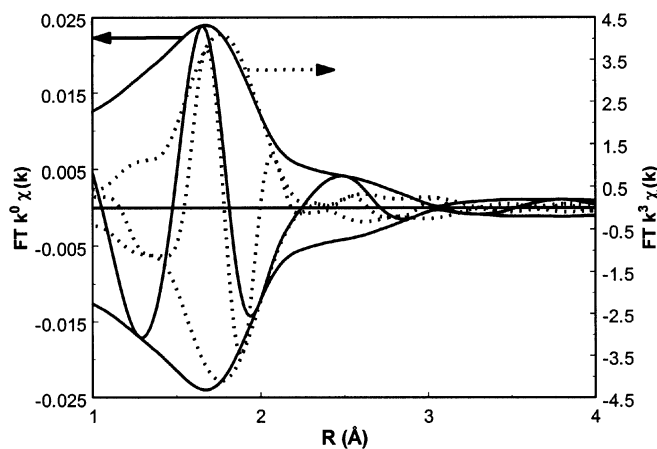


Figure 14. Fourier transforms of the EXAFS data of Copper-arene thiolate catalyst obtained at RT for $2.9 < k < 12.5 \text{ \AA}^{-1}$; k^0 -weighted (solid line) and k^3 -weighted (dotted line).

Table 1. Single Crystal X-ray Diffraction at 110 K and best obtained EXAFS fits^b on [Cu₃(SAr)₃].

Ab-Sc pair	N _{XRD}	R (Å) _{XRD}	N _{EXAFS}	R(Å) _{EXAFS}	Δσ ²	ΔE _o (eV)
Cu-N	1	2.08	1.0	2.05	0.001	0.6
Cu-S	2	2.21 (±0.02) ^a	1.9	2.23	0.003	-1.4
Cu...Cu	2	2.83 (±0.00) ^a	1.7	2.84	0.016	1.7
Cu...C ^a	3	2.96 (±0.02) ^a	3.3	2.99	0.013	7.9
Cu...C ^b	3	3.31 (±0.14) ^a	2.8	3.45	0.010	-1.3

^a In between brackets, the maximum deviation in distances is given.

^b k^0 variance 0.017 (Im) and 0.012 (Abs); k^3 variance 0.20 (Im) and 0.10 (Abs).

ering a found minimum to be acceptable was an equal fit quality in both k^0 - and k^3 weighting. When using a k^3 weighting as a starting point, many local minima were observed, which obscured the true minimum. The Cu-Cu shell, in particular, correlated highly with the Cu-C contributions, so that a decision on the final fit parameters could not be taken. Performing the fit using the lowest k weighting, the true minimum was detected. The fit quality using the k^3 weighting was equally good. The so-called difference file technique is used to explain this phenomenon. It allows the inspection of each individual contribution with respect to the other contribution in the EXAFS spectrum, including the difference between the total fit and the raw data. The experimental data can be regarded as a summation of several modulated EXAFS contributions ($\chi_{\text{MOD}_j}(k)$), describing each co-ordination shell:

$$\chi_{\text{EXP}}(k) = \sum_{j=1}^{\text{Shells}} \chi_{\text{MOD}_j}(k) \quad (23)$$

Each individual fitted contribution (shell m) can be described as the difference between the experimental data and all the other fitted contributions:

$$\chi_m = \chi_{\text{EXP}} - \sum_{i=1 \text{ and } i \neq m}^j \chi_{\text{MOD}_i} \quad (24)$$

The right side of this equation is denoted as the *difference file* of shell m . The experimental noise is represented on the right side of equation 24. Equation 24 enables a direct comparison of the single shells, and of each shell with the noise level in the experimental data.

The fitting of the K edge EXAFS of the Cu₃(SAr)₃ spectrum succeeded only when the lowest k weighting was used as a starting point. Figure 15 reveals the combined EXAFS contributions of the higher shells, viz. Cu-Cu, Cu-C^a and Cu-C^b with k^0 weighting. At higher k values, the intensity of the signal is rather flat and the oscillations have low intensity. This is the result of so-called anti-phase behavior. The sign of the Cu-Cu and Cu-C contributions is opposite at high k -values, thus canceling the intensity of each other. The oscillations have a high intensity at low k -values. Using a k^3 weighting, the small intensity oscillations are magnified, making the k^3 -weighted EXAFS spectrum insensitive to and less accurate for the Cu-Cu and Cu-C contributions. This explains the observed number of local minima and the difficulty in finding the true minimum in the k^3 weighting.

The k^3 -weighted Fourier transform in Figure 14 reveals a near zero signal around 2.2 Å, reflecting the damping of the

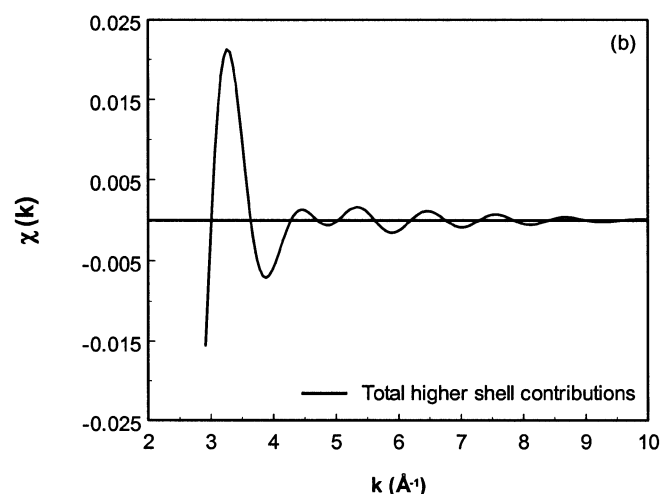


Figure 15. EXAFS signal of the Cu-Cu, Cu-C^a and Cu-C^b contributions, showing destructive interference at the higher k values, leading to a structureless EXAFS signal with small oscillations.

Cu-Cu and Cu-C signals, which are all significantly intense at this distance. The k^0 -weighted Fourier transform clearly shows the intensity in this range, indicating that when this k weighting is used as a starting point, the chance of success is largest [22]. Principally, any fit should be correct in every k weighting applied. The example discussed above proves that when different k weightings are used, the detection of a local minimum is facilitated. Careful observation of the Fourier transforms using low and high k weightings suggests the presence of anti-phase behavior through the lack of intensity in only one k weighting (that can be the high or low weighting). Moreover, as shown in Figure 11, when only one k weighting is used, contributions present in the EXAFS signal might be obscured, thus emphasizing the necessity of applying different k weightings.

2.8.6. R Space Versus k Space Fitting

The procedure used to analyze EXAFS data in k space was discussed above: a spectrum is Fourier-filtered by making a Fourier back transformation of a limited range in R space. Fitting in R space relies on the same mathematics, but in R space, thus eliminating the back Fourier transformation step. In k space fitting, a single shell, or at least a few shells, are separated from other higher shell contributions. A consequence of this procedure is that the reliable k -range becomes smaller due to truncation errors [23], thus lowering the number of independent parameters (equation 20). This is unfavorable. A second major concern in fitting in k space is the choice of R_{\min} and R_{\max} in setting the ranges of Fourier filtering (Figure 10). The presence of clearly separated peaks in a Fourier transform cannot be simply interpreted as the presence of nicely separated shells. The Fourier transform of the k^3 -weighted spectrum of Cu₃(SAr)₃ (Figure 14) shows near-zero intensity at about 2.2 Å, which might be a choice of R_{\max} for making a reversed Fourier transform. However, as argued above, three shells contribute to the signal in this range. As a consequence, a back-transformed contribution may not repre-

sent an entire single shell and it may contain parts of additional shells. These unwanted contributions are present over the whole k -range of the back-transformed EXAFS signal, thus making these contributions difficult to identify. Fitting in R space enables the direct observation of the partially overlapping higher shell contributions, thus decreasing the chance of interpreting the data incorrectly. A contribution (a peak) of a single shell in a Fourier transform may not be reflected as a nice symmetric peak.[#] In Fourier filtering for fitting in k space, the low frequency noise can increase, although the contributions of higher shells and the high-frequency noise are eliminated.

3. DESCRIPTION OF *IN-SITU* CELLS FOR EXAFS FOR CATALYTIC PURPOSES

As described in literature, there are many types of *in-situ* cells for XAS measurements. Depending on the aim of the research, unique and experiment-specific set-ups have been designed. Examples are set-ups for extreme high temperatures and pressures, using capillaries [32] or diamond anvil cells [33], for liquid samples or supercritical fluids [34], or in the presence of (corrosive) gasses. A number of designs for electrodes in electrochemical cells have also been designed [35]. The overview given here is limited to an extremely small number of experimental cells for XAS measurements of catalysts under pre-treatment and actual catalytic conditions, thus at high temperature, non-vacuum pressures, and in the presence of a reacting gas.

In-situ cells should protect the ambient or the vacuum conditions of a XAS beamline from the harsh environment on the sample, while maintaining X-ray transparency. This requires a protective material that can withstand differences in pressure and temperature, while being inert to any corrosive gasses. Moreover, the materials used in the reaction chamber should not be catalytically active.

Two types of cells are described here: type I has a chamber, through which a reacting gas flows, surrounding a heated sample, and type II represents a true plug-flow reactor. Each design has advantages.

3.1. Type I: Treatment Chamber Cells

The first *in-situ* cell for catalytic research was probably described by Lytle et al. [36] as early as 1979. A powdered sample is kept inside a beryllium or boronitride boat, enabling measurements at temperatures up to 773 K at ambient pressure. Boronitride windows separate the sample from a volume in a hollow aluminium cube that can be evacuated. Since this early design, many similar devices have been developed. Here, the revised version of a cell [37] used by several research groups throughout the world is presented (Figure 16). This cell contains a sample pressed into a self-supporting wafer in a rectangular opening in a flat cylindrical inox sample holder (a). The thickness of the sample holder can be adjusted

[#] Application of phase- and amplitude-corrected Fourier transforms represents a single contribution as a symmetric peak in the Fourier transform with the imaginary and absolute part peaking at the true distance R .

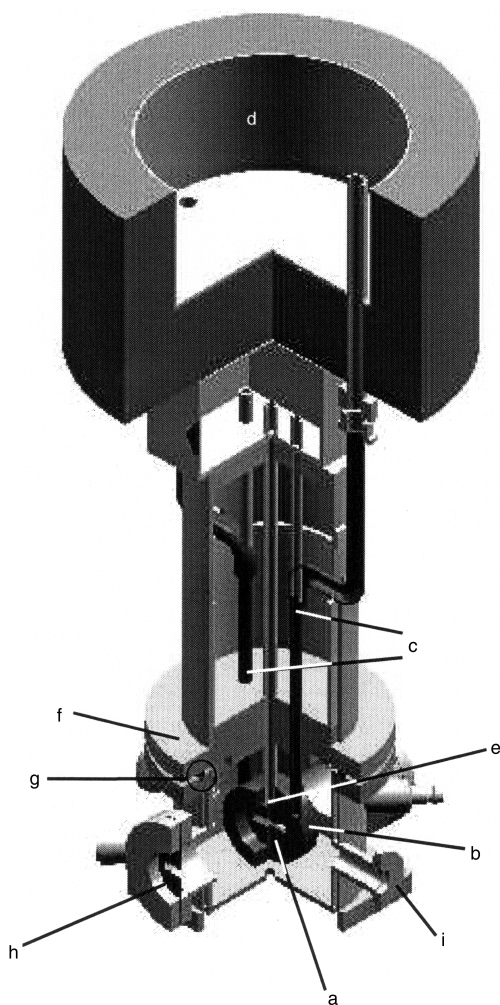


Figure 16. *In-situ* cell using a pressed pellet and an *in-situ* chamber, which functions as a continuously stirred tank reactor: a) sample holder; b) heater/cooler cylinder; c) hollow tubes for coolant liquid and electrical wires; d) reservoir for coolant liquid; e) thermo-couple; f) flange topping the *in-situ* chamber; g) O-ring; h) X-ray transparent window material; i) gas inlet/outlet taps.

to match the amount of sample needed for a XAS experiment. Pressed wafers ensure homogeneity of the sample and prevent radiation leaks. The stainless steel sample holder fits precisely into a stainless steel heater/cooler cylinder (b). Within this cylinder, a coiled heating wire enables heating of the sample up to 773 K. Moreover, the cylinder is hollow, with joints (c) that permit flowing of liquid nitrogen (or any coolant liquid), contained in a container on top of the cell, part of which is shown (d). Boiling of the liquid nitrogen in the hollow cylinder ensures a continuous flux of liquid nitrogen and guarantees a temperature of approximately 77 K on the sample. A thermocouple (e) inside the cylinder on top of the sample holder accurately measures the temperature of the sample, though calibration is necessary. The cylinder (b) is welded onto a flange (f) on top of the stainless-steel *in-situ* chamber. An O-ring seal (g) ensures a vacuum-tight connection between the flange and the chamber. The chamber is equipped with two replaceable beryllium windows (h). If desirable, windows of other materials can easily be mounted. Gas inlet and outlet

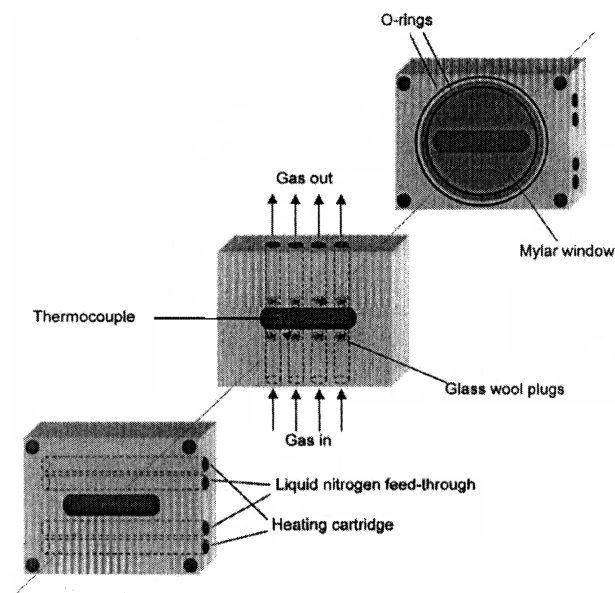


Figure 17. *In-situ* cell that permits XAS measurement under actual true catalytic conditions.

taps (i) are placed diagonally over the sample. To prevent heating and/or cooling of the beryllium windows when the sample is heated or cooled, water flows through the space between the double walls of the chamber, thus maintaining moderate temperatures around the chamber and the windows.

The sample temperature range in this cell is 77 to 773 K in various aggressive atmospheres (H_2 , H_2S , O_2 and CO), and the pressure range is 10^{-4} to $1.5 \cdot 10^3$ mbar or higher, depending on the window material used. The chamber functions as a continuously stirred tank reactor (CSTR), which performs well due to considerable turbulence inside the *in-situ* chamber, especially when there is a large difference between the temperature of the sample holder and that of the chamber wall. However, the large volume of the chamber prevents rapid changes in gas composition. The volume of newer designs is significantly smaller. The result is an elongated tube, through which the X-rays traverse. The diameter of the tube is decreased as far as possible, diminishing the dead volume significantly [38]. In all cases, however, the sensitivity of window materials to temperature requires the presence of a heat-resistant volume and/or cooled flanges, which limits not only the minimal size of the cell, but also the range of temperature and pressure that can be applied.

A cell was designed [39] with the goal of minimizing the effect of mass flow limitations, enabling measurements while performing actual catalytic reactions (Figure 17). A powdered catalyst is contained in between glass wool plugs. The reactant gas flows through the gas wool plugs over the powdered catalyst. At the outlet, a tube connected to a gas chromatograph (GC) enables detection of the gas effluent. Mylar windows are placed on both sides and ensure X-ray transparency and leak tightness. They also limit the maximum temperature to about 470 K at pressures up to 3 bars. Kinetic measurements under catalytic conditions showed very similar performance of the same catalyst placed in a plug-flow reactor.

3.2. Type II: True Reactor Cell

Type II *in-situ* cells are actually plug-flow reactors [32]. The heart of the cell consists of a capillary packed with catalyst particles. Placing the capillary inside a furnace (or passing hot gas over the capillary), with the catalyst in a stream of gas, enables measurements at high temperature and high pressure. Monitoring the gas effluent using a GC or mass spectrometer provides simultaneous information about the composition of the gas at the outlet of the catalyst bed. The material must be X-ray transparent and withstand high temperature and pressure, as well as resistance to corrosion by the reactants. Quartz and carbon fulfill these requirements and are frequently used materials. Furthermore, a capillary tube enables the detection of X-ray diffraction (XRD) by means of a position-sensitive detector that encircles the sample. This provides simultaneous long-range and short-range information. Figure 18 shows the set-up designed by the group of professor J. M. Thomas. The figure shows the possibility of measurements in transmission and fluorescence mode, if the sample is too thick or the element under study is too dilute [32, 40]. In the figure, the sample holder can be used for measuring a solid-liquid heterogeneous system, however, placing a capillary allows measurement of solid-gas catalytic systems.

In the case of capillaries, the X-ray beam 'spot' will be rectangular shaped with a low height and a high width in order to have a sufficient photon count. In this type of design, care should be taken that the complete X-ray beam is measuring catalyst particles at identical conditions, because the gas composition at the inlet and outlet differs due to the catalytic conversion. Consequently, a catalyst particle at the gas inlet may observe a different gas composition than one at the outlet. Working under differential conditions (at very low conversions) resolves this problem. Moreover, the catalyst bed must be packed carefully, giving a homogeneous distribution of catalyst particles.

3.2.1. Fluorescence & Electron Yield Detection Compatibility

The designs described above are mostly designed for transmission measurements, however, small adaptations to the set-ups allow fluorescence measurements, as illustrated in Figure 17. For the 'chamber type I designs', an additional exit win-

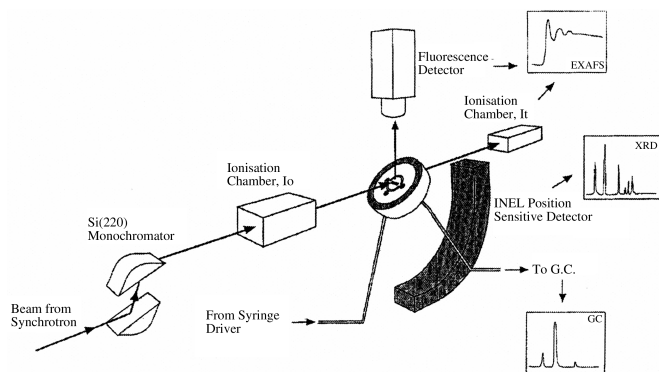


Figure 18. Set-up for parallel measurement of EXAFS and XRD, while measuring the performance of a catalyst by GC.

dow under an angle of 90 degrees with the X-ray beam must be constructed. Adjustment is relatively straightforward and can be done without satisfying the most severe measurement conditions.

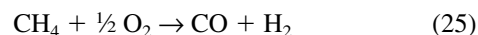
Electron yield detection is not frequently used for *in-situ* measurements in the hard X-ray regime. Nonetheless, successful examples of *in-situ* cells that employ electron yield detection for measurements of catalysts under gas atmospheres at high temperatures (max. reported 1000°C) and pressures (50 bar hydrogen at 500°C) have been described [41].

4. IN-SITU EXAFS FOR CATALYTIC APPLICATIONS

4.1. Catalytic Partial Oxidation

A good example of *in-situ* EXAFS under non-ambient conditions is given by the Haldor Topsøe group [42]. Using a quartz capillary tube, XAS measurements were performed under actual plug-flow conditions. Measurements were performed in transmission mode through ionization chambers.

The reaction under study is the catalytic partial oxidation (CPO) of natural gas (methane) to CO and H₂:



This reaction is the first step in gas-to-liquid (GTL) technology of methane. This potential technology should lead to liquid products such as CH₃OH (methanol), alkenes, and paraffinic or olefinic fuels. Many supported metal catalysts are probably suitable for performing this reaction. The system investigated by the Topsøe team is alumina-supported rhodium (Rh/Al₂O₃). Rhodium was the element of choice because of its low coking property. There is no agreement concerning the reaction mechanism, and the catalyst structure under reaction conditions is not yet understood. The latter was addressed by the Topsøe team using Rh K edge EXAFS (23,219.8 eV) in their *in-situ* capillary set-up (paragraph 3.2).

4.1.1. Strategy, Samples and Treatments

XAS Measurements were performed on the as-synthesized precursor catalyst, through several activation steps, to the actual catalytic measurements. Quick EXAFS was used during the temperature ramps to study the evolution of the system as a function of temperature and gas environment, measured on-line using a mass spectrometer. After the final temperature was reached and after cooling the sample to room temperature, normal EXAFS spectra were taken. In some cases, high-temperature measurements were also performed and the structure compared to the low-temperature measurements. The structure of the catalyst was related to the temperature and the composition of the gas.

4.1.2. Structure as Function of Gas Composition and Temperature

Figure 19 shows the Fourier transforms of (a) the fresh catalyst, (b) after treatment at 500°C in He, (c) after treatment at 500°C in H₂, and (d) for comparison a Rh foil. Clear differences in the intensity of the peaks are visible in the spectra. Table 2 (discussed below) gives the results of the EXAFS

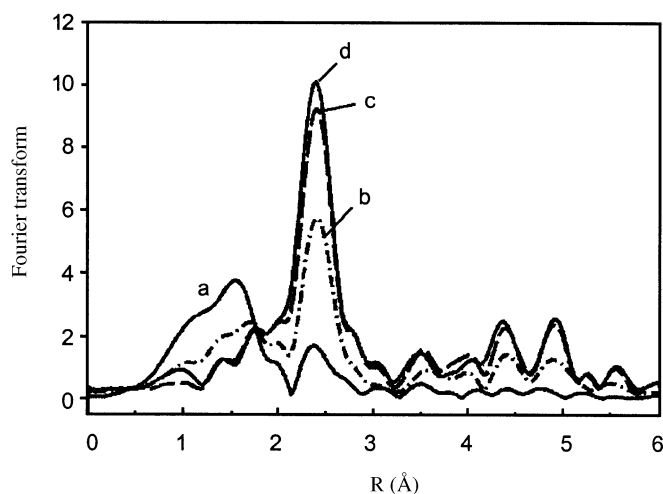


Figure 19. k^1 weigh-weighted Fourier transform of Rh K edge spectra of Rh/Al₂O₃ at room temperature: a) fresh catalyst, b) after treatment at 500°C in He (step A), c) after 500°C in H₂ (after step B), and d) Rh foil.

data analysis of spectra taken at room temperature after the respective treatments. Table 3 compares high-temperature and low-temperature measurements. Data analysis was performed through back-transformation of a filtered shell in a Fourier transform.

A 5wt% Rh-loaded catalyst was obtained by solid-liquid reaction of Rh₄(CO)₁₂ and α -Al₂O₃ dispersed in hexane under an atmosphere of CO. The EXAFS fitting shows that the coordination numbers of Rh-Rh and Rh-O/C (oxygen and carbon are very difficult to distinguish) are 2.0 at 2.67 Å and 3.2 at 2.00 Å, respectively. This indicates that the rhodium carbonyl structure more or less retained its structure. Heating this as-synthesized catalyst in helium followed by QEXAFS (not shown here) indicated that carbonyl decomposition starts at temperatures above 170°C. CO and CO₂ were monitored as decomposition products, while metallic particles formed. After decomposition at 500°C, a strong increase in the Rh-Rh coordination number (2.0 to 6.9 at 2.69 Å) and a slight decrease in Rh-O/C coordination number (3.2 to 2.0 at 2.07 Å),

Table 2. Fit parameters of the first two shells (O/C and Rh) for Rh K edge Rh/Al₂O₃ after heating in inert, reduction and reaction with CH₄/O₂.

Scatterer	6. N	σ (Å)	7. R (Å)	ΔE_0 (eV)	χ^2
<i>Rh/Al₂O₃, as synthesized</i>					
Rh-O/C	3.2	0.086	2.00	-0.5	0.0029
Rh-Rh ^a	2.0	0.09	2.67	1.3	0.010
<i>Rh/Al₂O₃, after heating in He (500°)</i>					
Rh-O/C	2.0	0.10	2.07	-5.0	0.016
Rh-Rh ^a	6.9	0.09	2.69	-1.8	0.0006
<i>Rh/Al₂O₃, after reduction in H₂ (500°)</i>					
Rh-O/C	1.5	0.10	2.12	-11	0.1
Rh-Rh ^a	10.3	0.09	2.69	-1.7	0.0009
<i>Rh/Al₂O₃, after heating in CH₄/O₂ (600°)</i>					
Rh-O/C	1.5	0.084	2.04	-0.1	0.0027
Rh-Rh ^a	9.3	0.09	2.69	-1.3	0.0007

^a Reported values for k^3 weighting.

Table 3. k^3 weighted fit parameters for the third shell (Rh) for Rh K edge Rh/Al₂O₃ after heating in inert, reduction and reaction with CH₄/O₂.

Scatterer	8. N	σ (Å)	9. R (Å)	ΔE_0 (eV)	χ^2
<i>Rh/Al₂O₃, as synthesized</i>					
Rh-Rh ₂	<i>no contribution detected</i>				
<i>Rh/Al₂O₃, after heating in He (500°)</i>					
Rh-Rh ₂	8.2	0.10	4.70	-4.5	0.023
<i>Rh/Al₂O₃, after heating in CH₄/O₂ (600°)</i>					
Rh-Rh ₂	8.9	0.09	4.68	0.1	0.0027
<i>Rh/Al₂O₃, in CH₄/O₂ at 600°</i>					
Rh-Rh ₂	4.4	0.12	4.68	0.1	0.29
<i>Rh/Al₂O₃, after reduction in H₂ (500°)</i>					
Rh-Rh ₂	10.6	0.09	4.69	-3.0	0.0036
<i>Rh/Al₂O₃, in H₂ at 500°</i>					
Rh-Rh ₂	7.5	0.08	4.69	-8.0	0.0066

indicate that particle growth occurs during this treatment (Table 3). The reduction in 2% H₂ in N₂ results in further particle growth. The QEXAFS measurement (not shown) performed during heating in 2% H₂ in N₂ indicated that all the rhodium atoms were in the reduced state at temperatures above 175°C. Large coordination numbers (10.3) at the bulk metal distance of 2.69 Å were found after cooling the sample to room temperature, but a low oxidic coordination number was also detected.

After the reduction, the Rh catalyst was exposed to a typical reaction mixture of 6% CH₄/3% O₂/He. It was shown with *in-situ* QEXAFS that, starting at room temperature, the structure of the catalyst gradually oxidizes as the temperature increases. However, at a temperature of approximately 320–330°C and a residence time of 0.54 seconds, the catalyst changes abruptly to the reduced state. This is the same temperature at which the reaction ignited, as shown by the MS analysis. This clearly indicates that the structure of the catalyst depends strongly on the composition of the gas as a function of temperature. Moreover, the experiments of Topsøe et al. prove that, under conditions at which the rhodium particles are active, the catalyst has metallic character. After cooling the catalyst (in a flow of the reaction mixture), the room temperature measurement does not indicate large changes in the structure compared to the reduced state; high Rh-Rh coordination numbers are found (10.3 vs. 9.3).

4.1.3. High-Temperature versus Low-Temperature Measurements

A measurement at high temperature showed large changes in the EXAFS parameters. The authors clearly showed this change by providing the fit parameters of the second Rh-Rh₂ coordination shell (Table 3), visible for the size of particles in their study. Measurement at room temperature after heating in the reaction mixture showed a coordination number of 8.9 for this second Rh-Rh₂ coordination shell, whereas measurement at 600°C decreased this value to 4.4 at an identical Rh-Rh₂ distance of 4.68 Å. In addition, the first Rh-Rh coordination shell in the Fourier transform decreased strongly in intensity (Figure 20). Although no fit parameters of this first Rh-Rh shell were provided, the results were interpreted as a

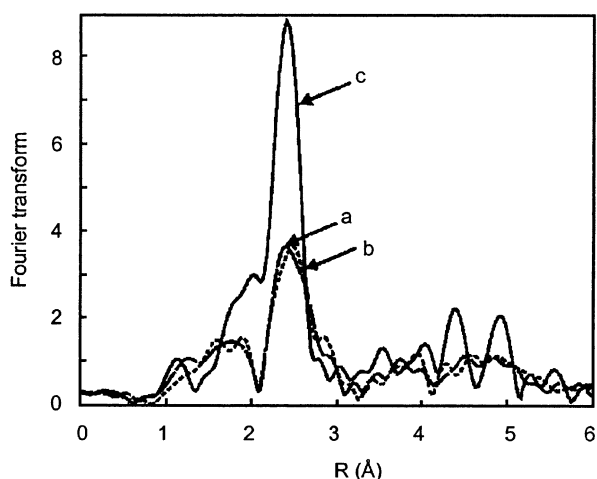


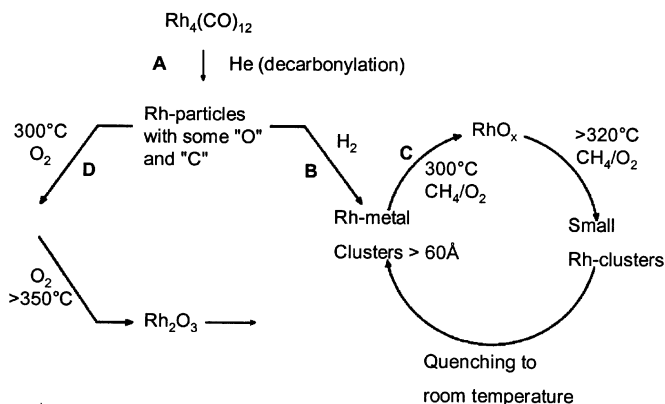
Figure 20. k^1 weigh-weighted Fourier transforms of Rh K edge spectra of Rh/Al₂O₃ during: a) treatment at 600°C in CH₄/O₂ (step C, 12 ml/min), b) treatment in CH₄/O₂ (step C, 1 ml/min), and c) during treatment in H₂ at 500°C (step B).

re-dispersion of the rhodium metal particles. It was claimed that this process is reversible with respect to temperature in several cycles. Cooling to room temperature led to a return of the catalyst to a close proximity of its initial state prior to treatment, i.e., large Rh particles. Measurement at high temperature under hydrogen (2% in N₂) showed a similar decrease in particle size. However, the coordination number of the second Rh-Rh₂ shell decreased less strongly (10.6 vs. 7.5) than in the case of the reaction mixture (8.9 to 4.4).

The authors did not mention the possibility of asymmetric distribution functions in the high-temperature measurements, which may influence the fit results. However, the fits of spectra taken at high temperature all show virtually identical Rh-Rh₂ distances, which suggests that asymmetric distribution functions do not play a major role.

4.1.4. State of Rhodium in Rh/Al₂O₃

A detailed interpretation of the EXAFS data obtained under the different conditions led to the following scheme (1) of the evolution of the structure of the 5 wt% Rh/Al₂O₃ as a function of temperature and gas environment:



Scheme 1. Structural changes during treatments to CPO catalyst Rh/Al₂O₃.

The as-synthesized catalyst, Rh₄(CO)₁₂, undergoes decarbonylation (step A) during heating in helium and forms small rhodium particles (CN = 6.9). A reduction in hydrogen (step B) gives bigger rhodium metal particles (CN = 10.3), whereas oxidation (step C, not mentioned in Tables 2 and 3) gives rhodium oxide particles, which transform to rhodium metal clusters when treated in methane (step E, not mentioned in Tables 2 and 3). The rhodium particles slowly oxidize in the reaction mixture of CH₄ and O₂ at temperatures up to 320°C, at which point rhodium metal forms. This was the same temperature at which the reaction ignited. The dimensions of the metal particles at this high temperature are lower than after quenching to room temperature, interpreted by the authors as a re-dispersion of the metallic rhodium particles.

4.1.5. Conclusion

In this *in-situ* EXAFS study, the authors determined the structure of the CPO catalyst under reaction conditions. It was shown that the structure of the catalyst changes abruptly at the temperature at which the reaction ignites (change from an oxidic to a reduced state).

Moreover, this example shows that the structure of an active catalyst may depend strongly on the conditions under which the measurement is performed and that freezing a sample after high-temperature treatment will not necessarily maintain it in that state [5].

4.2. Structure and Nature of Active Sites in Hydrotreating Catalysts

Koningsberger et al. [43] give another typical example of *in-situ* EXAFS used in the investigation of catalytic systems, i.e., sulfided cobalt-promoted molybdenum catalyst supported on alumina, Co-Mo/Al₂O₃, a well-known hydrotreating catalyst. In modern refineries, the petroleum feedstock is hydrotreated, and so-called hydrodesulfurization (HDS) (and hydrodenitrogenation, HDN) processes remove sulfur (and nitrogen) from the feed. Compounds containing these elements poison catalysts downstream in the refinery process and are undesirable products in gasoline due to the harmful SO₂ exhausts. A third advantage of S removal is the improvement in the quality of the gasoline (colour, odour, stability and corrosion). Many in-depth studies of the structure of the active site in HDS (and HDN) catalysts have been carried out with supported sulfided metal catalysts such as molybdenum-sulfides supported on alumina. There is general agreement about the structure of the molybdenum sulfides. One or more slabs of molybdenum atoms, sandwiched between layers of sulfur atoms, form on the support. Catalytic activity is improved by adding promoters like cobalt and/or nickel. Several studies on the Co, Ni and Mo edges have been published, providing information about the structure of the catalyst and the structure of the active site. Probe reactions such as the desulfurization of thiophene are often used in academic catalytic studies. In thiophene, a sulfur atom with four CH-groups make up a closed ring, with each carbon atom involved in one double bond (Figure 21). In the EXAFS study described here, a structural analogue of thiophene, namely selenophene, was used. It has the same structure as thiophene, except that a selenium atom replaces the sulfur. It is expected that this Se-containing hydrocarbon ring

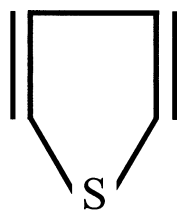


Figure 21. Structure of thiophene.

displays similar chemistry as thiophene, because Se is positioned directly below S in the Periodic Table. This is indeed observed when the two probe molecules were compared in kinetic measurements, although selenophene proved to be slightly more active. Use of this ‘heavy-atom’ structural analogue enables the study of the catalyst, from *the point of view of the reactant*, by measuring the Se K edge EXAFS signal. The difference in size of the three large elements in the catalytic system (Co, Mo and Se) is large enough to distinguish them as neighbouring atoms in an EXAFS experiment. Thus, a very powerful experimental tool exists for studying the catalytic HDS process. The structure of the catalyst is being studied at the Mo and Co K edges (at 20000 and 7709 eV, respectively), and the reacting molecule and its decomposition can be studied at the Se K edge (12658 eV). This complementary information enables studying of the interaction of the reactant with the catalyst and the envelope of the catalyst structure during the HD-Se reaction. Moreover, the incorporation of the Se-atoms into the Co-Mo-sulfide particles can be followed. During the kinetic measurements of selenophene, it was found that the Se-atoms were incorporated into the Mo-sulfide slabs.

4.2.1. Strategy, Samples and Treatments

In this study, EXAFS was again used to study all consecutive treatment steps, including the actual reaction conditions. The authors performed EXAFS measurements at the Mo, Co and Se edges under identical conditions, and obtained complementary information.

A 15 wt% MoO₃/Al₂O₃ catalyst (referred to as Mo/Al₂O₃) was synthesized using incipient wetness impregnation of (NH₄)₆Mo₇O₂₄·6H₂O on γ-Al₂O₃ (200 m²/g). A cobalt promoted catalyst (called Co-Mo/Al₂O₃), with loadings of 3.8 wt% Co₃O₄ and 14 wt% MoO₃, was synthesized by in-

ipient wetness co-impregnation of (NH₄)₆Mo₇O₂₄·6H₂O and Co(NO₃)₂·6H₂O on γ-Al₂O₃. In addition, a commercial cobalt-promoted Mo/Al₂O₃ catalyst was used (*com-Co-Mo/Al₂O₃*) (KT752 from AKZO).

Table 4 lists treatments and measurement conditions. Measurements were performed after the treatments, immediately followed by another treatment and measurement. Samples are pressed into self-supporting wafers and the *in-situ* cell, described in paragraph 3.1, was used. The data analysis procedure included fitting in R space and applying the difference file technique as described in paragraph 2.8.

Due to the highly toxic nature of reaction products, H₂Se and Se, *in-situ* experiments were not performed using selenophene at reaction temperature. The reaction mixture was, however, quenched with He at 423 K before EXAFS measurement at the liquid-nitrogen temperature. During this treatment, physisorbed species are desorbed, while the chemisorbed species remain on the surface.

4.2.2. Genesis of Active Sites

The influence of consecutive sulfidation, reduction and thiophene/H₂ reaction on Mo/Al₂O₃ and the promoted catalyst, Co-Mo/Al₂O₃, was examined to determine whether the promotion with cobalt influences the creation of vacancies.

Figure 22a shows the results of the Co K edge measurements. It shows the absolute part of the Fourier transform of the Co-Mo/Al₂O₃ catalyst after it was sulfided (solid line), reduced (dotted line) and exposed to thiophene/H₂ (dashed-dotted). A major contribution is visible at around 1.5 Å and a small peak near 2.8 Å. Fitting of the spectra (Table 5) showed that the main peak is basically due to Co-S scattering and the latter to interference of two different Co-Co and one Co-Mo scattering pairs. The reduction (dotted line) causes a small decrease in the intensity of the main Co-S peak, followed by a slight increase after treatment with thiophene. Figure 22b shows both the imaginary and absolute part of the sulfided Co-Mo/Al₂O₃ catalyst after reduction with H₂ and the best fit. An excellent fit is visible in the range 0.75 < R < 3.75 Å in both the absolute and the imaginary parts. This is also reflected in the reported variances in imaginary and absolute parts of the Fourier transform. Table 5 gives the results of the fitting. After sulfidation, the Co atoms are surrounded by an average of six sulfur atoms, decreasing to N = 5.2 in hydrogen, a significant loss of almost one neighbour. In the thiophene/H₂ mixture, the coordination number only slightly

Table 4. Treatment and measurement conditions for the HDS catalysts.

Treatment	Drying/calcination	Sulfidation	Reduction	Reaction	Reaction
Gas	Air	10% H ₂ S/H ₂	H ₂	thiophene ^a /H ₂	selenophene ^a /H ₂
Temperature, Duration	298K, 4hr; 383K, 6hr; 723K, 16hr.	673 K, 30 min	673 K	673K, 1hr ^b	-673K, 1hr; -473K, 1hr
Measurement Condition	n.d.	-673 K, H ₂ S/H ₂ ^c -77 K, H ₂ S/H ₂	673 K, H ₂	673 K, thiophene/H ₂	77 K
K Edge	n.d.	Co, Mo	Co, Mo	Co, Mo	Co, Mo, Se ^d

^a 2 Vol% in H₂.

^b First cooled to 298 K before heating to measurement temperature.

^c Measurement at other temperatures gave same results.

^d Edges were measured at 77 K after a flush with He at 423 K.

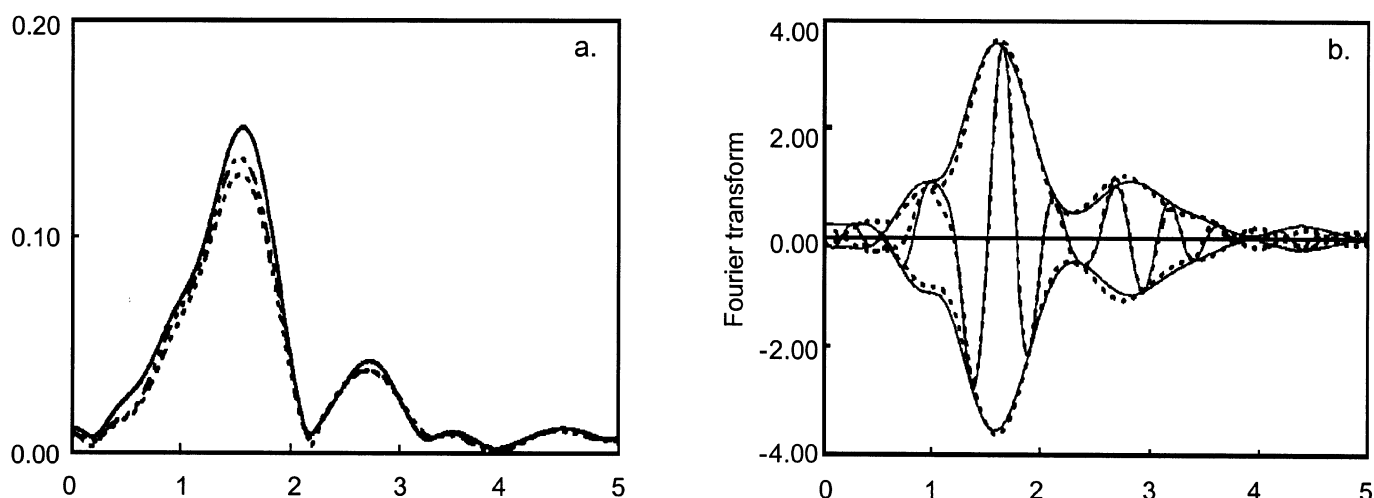


Figure 22. a) Absolute part of the Fourier transform of the Co K edge EXAFS of the Co-Mo/Al₂O₃ catalyst sulphided (solid line), after reduction (dotted line) and after exposure to thiophene/H₂ (dashed-dotted line) (k^3 weighted, $3.0 < k < 10.0$); b) The imaginary part of the sulphided Co-Mo/Al₂O₃ catalyst after reduction with H₂ and the best obtained fit (k^3 weighted, $3.0 < k < 10$).

increases to $N = 5.4$, still significantly lower than after the sulfidation.

The fitting of the spectra taken at the Mo K edge in Mo/Al₂O₃ give different results (Figure not shown). The sulfided Mo/Al₂O₃ catalyst has an average of five sulfur neighbours as well as half an oxygen neighbour (Table 6). This oxygen contribution is assigned to oxygen in the alumina support, binding the molybdenum sulfide slabs to the support. Note, no contribution of oxygen of the support was found for cobalt, proving that cobalt is not involved in bonding to the Al₂O₃ support. The reduction in hydrogen causes a very small decrease in the coordination number of sulfur, hardly more than the error of measurement. Again, no significant changes occurred after the addition of thiophene to the feed.

Table 5. Fit parameters Co K edge for Co-Mo/Al₂O₃ after sulfidation, reduction and reaction with thiophene.

Scatterer	10. N	$\Delta\sigma^2$ (10^{-4} \AA^2)	11. R (\AA)	ΔE_0 (eV)	Var. Im. ^a	Var. Ab. ^b
<i>Co-Mo/Al₂O₃ Sulphided 673 K, k^3</i>						
Co-S	6.0	94.6	2.16	9.7	0.66	0.21
Co-Co	1.5	110.1	2.42	-1.0		
Co-Mo	1.2	81.4	2.77	6.2		
Co-Co	2.9	4.2	3.47	10.0		
<i>Co-Mo/Al₂O₃ Reduction H₂ 673 K, k^3</i>						
Co-S	5.2	88.5	2.16	9.8	1.90	0.52
Co-Co	1.4	1.2	2.38	-1.0		
Co-Mo	1.2	74.2	2.75	6.3		
Co-Co	2.6	32.5	3.47	10.0		
<i>Co-Mo/Al₂O₃ Thiophene/H₂ 673 K, k^3</i>						
Co-S	5.4	89.3	2.16	10.0	2.01	0.80
Co-Co	1.3	108.9	2.38	1.1		
Co-Mo	1.4	67.6	2.75	7.1		
Co-Co	2.7	25.8	3.47	9.8		

^a Variance imaginary part Fourier transform.

^b Variance absolute part Fourier transform.

The authors interpret the decrease in the Co-S coordination number after reduction as a result of the creation of sulfur vacancies, preferentially on the Co atoms, not observed in the Mo/Al₂O₃ catalyst. These EXAFS results confirmed other reported assumptions. The authors also suggest that the different response to the reduction of the (sulfided) Mo/Al₂O₃ and Co-Mo/Al₂O₃ catalysts will result in *different* active sites in these two catalysts. Thus, Co-promotion not only enhances the *number* of active sites by creation of vacancies at 673 K, it also alters the *nature* of the active sites by formation of a different vacant site compared to the unpromoted Mo/Al₂O₃.

The presence of Co-Co coordination shells at 2.42 and 3.47 \AA , respectively, in Co-Mo/Al₂O₃ is assumed to be due to the creation of a small amount of a bulk-like cobalt sulfide (Co₉S₈) that forms during the synthesis and mixes with the desired 'Co-Mo-S' phase. Measurement of the *com*-Co-Mo/Al₂O₃ catalyst at the Co K edge did not reveal the pres-

Table 6. Fit parameters Mo K edge for Mo/Al₂O₃ after sulfidation, reduction and reaction with thiophene/H₂.

Scatterer	12. N	$\Delta\sigma^2$ (10^{-4} \AA^2)	13. R (\AA)	ΔE_0 (eV)	Var. Im. ^a	Var. Ab. ^b
<i>Mo/Al₂O₃ Sulphided 673 K, k^2</i>						
Mo-O	0.5	84.7	1.99	0.9	0.81	0.51
Mo-S	5.0	49.8	2.41	1.8		
Mo-Mo	2.9	76.0	3.16	2.2		
<i>Mo/Al₂O₃ Reduction H₂ 673 K, k^2</i>						
Mo-O	0.5	91.7	1.99	5.0	0.90	0.56
Mo-S	4.8	53.7	2.41	1.4		
Mo-Mo	2.8	84.1	3.16	2.5		
<i>Mo/Al₂O₃ Thiophene/H₂ 673 K, k^2</i>						
Mo-O	0.5	101.6	1.99	0.7	0.67	0.42
Mo-S	5.1	47.6	2.41	2.0		
Mo-Mo	3.1	74.2	3.16	2.3		

^a Variance imaginary part Fourier transform.

^b Variance absolute part Fourier transform.

Table 7. Fit parameters Se, Co and Mo K edges for *com*-Co-Mo/Al₂O₃ after reaction with Selenophene/H₂.

Scatterer	14. N	$\Delta\sigma^2$ (10 ⁻⁴ Å ²)	15. R (Å)	ΔE_0 (eV)	Var. Im. ^a	Var. Ab. ^b
<i>Se K edge, com-Co-Mo/Al₂O₃ HD-Se 473 K, k¹</i>						
Se-C	1.0	36.5	1.71	-6.9	1.13	0.48
Se-Co	1.0	10.7	2.39	-5.6		
Se-S	0.8	64.2	2.89	1.3		
<i>Se K edge, com-Co-Mo/Al₂O₃ HD-Se 673 K, k¹</i>						
Se-Co	1.0	14.0	2.35	-9.1	0.42	0.26
Se-Mo	1.0	16.1	2.55	-7.9		
Se-S	0.3	18.8	3.15	-2.4		
Se-Se	0.5	70.1	3.28	-6.5		
Se-Se	4.5	183.4	4.10	8.01		
<i>Co K edge, com-Co-Mo/Al₂O₃ HD-Se 673 K, k³</i>						
Co-S	1.8	-25.4	2.20	4.5	1.06	0.47
Co-Se	1.9	16.3	2.35	-4.4		
Co-Mo	1.4	-3.8	3.28	-2.6		
<i>Mo K edge, com-Co-Mo/Al₂O₃ HD-Se 673 K, k²</i>						
Mo-S	5.3	31.4	2.43	-0.5	0.50	0.25
Mo-Se	1.1	16.0	2.52	-5.7		
Mo-Mo	2.9	22.6	3.16	2.6		

^a Variance imaginary part Fourier transform.^b Variance absolute part Fourier transform.

ence of the two Co-Co coordination shells at 2.42 and 3.47 Å, respectively. This difference is due to the optimised synthesis of the commercial catalyst.

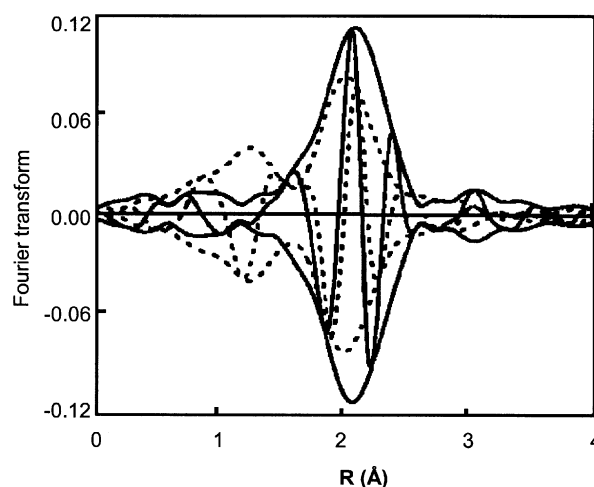
4.2.3. The Active Site as a Function of Temperature

The authors further investigated the nature of the active sites in Mo/Al₂O₃ and *com*-Co-Mo/Al₂O₃; only the latter is discussed here. Differences between active sites at 473 K and at 673 K were found. Table 4.3 shows the respective treatments; Table 7 gives the EXAFS fitting results of Se, Mo and Co K edge measurements.

4.2.4. Se K Edge 473 K, Low-Temperature HD-Se

Figure 23 shows the Fourier transform of the spectrum taken at the Se K edge of the sulfided *com*-Co-Mo/Al₂O₃ catalyst after the HD-Se reaction at 473 K (dotted line) and 673 K (solid line), respectively. The spectra were taken at 77 K after flushing with helium at 423 K. Clear differences in the spectra are visible. A k^1 weighting during the Fourier transformation emphasized the contribution of the light C scatterer, visible in the dotted line at $R = 1.2$. This peak disappeared after the reaction at 673 K, and the main peak shifted to higher R and became more intense. Moreover, the imaginary parts are clearly different. Fitting of the EXAFS data (Table 7) revealed that, after the low-temperature treatment, the first peak is due to a Se-C contribution at 1.71 Å and the main large peak at 2.0 Å to a single Co neighbour at 2.39 Å. The duration of the HD-Se reaction did not influence the local structure around the selenium atoms: only the height of the selenium edge increased, indicating that more Se-atoms were incorporated into the structure, while the fit parameters did not change dramatically.

The Se-C coordination number of $N = 1$ suggests that about half of the selenium atoms are still bound to the hydrocarbon ring. The Se-Co coordination number of $N = 1$ was

**Figure 23.** Fourier transforms of the Se K edge EXAFS of sulfided *com*-Co-Mo/Al₂O₃ catalyst after the HD-Se reaction at 473 K (dotted line) and 673 K (solid line), respectively (k^1 weigh-weighted $3.4 < k < 14.0$).

interpreted as the sorption of selenophene as a terminal ligand on the Co atoms located at the edges. Sorption on bridging sites was excluded, because in that case, Mo neighbouring atoms would have been observed as well.

4.2.5. Se K Edge 673 K, High-Temperature HD-Se

After the HD-Se reaction at 673 K, the structure around the selenium atoms in *com*-Co-Mo/Al₂O₃ changed compared to the low-temperature reaction (Figure 22). As mentioned above, the intensity of the amplitude at $R = 1.2$ Å due to the Se-C contribution is much lower. The intensity of the main peak increased, and clear differences in the imaginary part are visible, suggesting completely different contributions. These changes are reflected in the fit parameters (Table 7), indicating a complete loss of the Se-C contribution. In addition to the Se-Co scatterer pair (at 2.35 Å), an additional Se-Mo scatterer pair was observed at a distance $R = 2.55$ Å. Higher shells of S and Se atoms were also detected. Figure 24 shows Fourier transforms of Co K edge EXAFS of the sulfided (dotted line) *com*-Co-Mo/Al₂O₃ catalysts and after HD-Se (solid line). The main peak has a higher amplitude after reaction with selenophene. The Fourier transforms of the spectra taken at the Mo K edge (not shown here) show a similarly high intensity of the main peak after HD-Se, although the effect is somewhat less pronounced. Table 7 also shows the results of the fit at both the Co and Mo edges. Co-Se scattering was observed at $R = 2.35$ Å at the Co K edge, Mo-Se scattering at $R = 2.52$ Å at the Mo K edge. These distances correspond to the distances measured at the Se K edge, providing consistent information from the measurements at the different K edges. The Debye-Waller factors are also very similar, when both sides of the scatterer pairs are considered.

The different structure after the high-temperature HD-Se reaction is considered to be due to a different reaction mechanism compared to the low-temperature reaction. The absence of the Se-C coordination indicates that the Se-hydrocarbon ring is no longer present, hence, the Se-C bond breaking is no longer the rate-limiting step in the reaction. Moreover, the Se

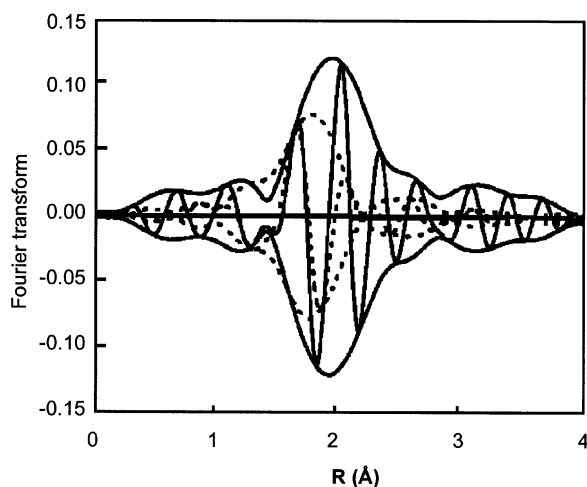


Figure 24. Fourier transforms of EXAFS of sulfided (dotted line) com-Co-Mo/ Al_2O_3 and after HD-Se (solid line) (k^3 weigh-weighted, $3.0 < k < 12.0$).

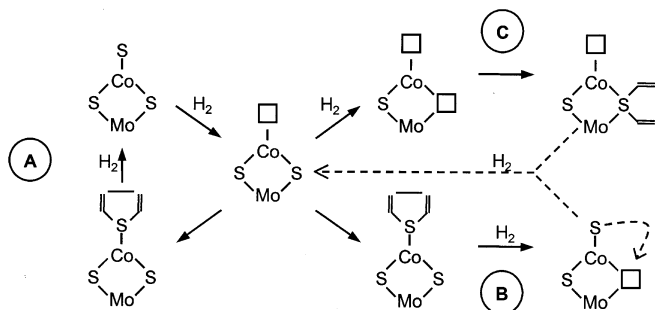
coordination to both Mo and Co atoms (with coordination numbers of 1) suggests that the Se atoms are now at bridging positions between these two elements, in contrast to the low-temperature reaction, where the Se atoms adsorb on top of a single Co atom. The bridging position of the selenium atom is also strongly suggested by the increase in the Co-Mo distance (Table 7) from 2.81 to 3.28 Å. The larger selenium atoms that replace the smaller sulfur atoms push the cobalt and molybdenum atoms further apart.

Systematic EXAFS measurement at increasing temperatures and analysis of the data indicated that the observed variation in coordination sphere of the different atoms is not due to the occurrence of asymmetric distribution functions at the highest temperatures.

4.2.6. Model of Reaction Scheme in HDS Reactions

Structural analogues of reacting molecules containing heavy elements like Se in selenophene provide a unique tool for studying the development and evolution of active sites in HDS reactions (the reaction described here). EXAFS measurements of the three different heavy elements in the catalyst provide a set of unique and complementary data that enabled the elucidation of the rate-limiting steps and catalyst structure in the HDS process at different temperatures.

A reaction scheme (2) of the HDS reaction is given below:



Scheme 2. Reaction scheme of hydro-desulphurization of thiophene.

The active HDS site at 473 K was identified as being a terminal sulfur vacancy (the square in the scheme) at a single Co atom in the “Co-Mo-S” structure. Selenophene is chemisorbed on cobalt, hydrogenated and released as H_2Se (route A in scheme 2). At 473 K, the scission of the Se-C bond is a slow process in comparison with the generation of the active sites (the sulfur vacancies), giving Se-C bonds in the Se K edge at this temperature (Table 7).

After treatment at high temperature (673 K), the EXAFS analysis shows that part of the Se atoms is placed in a bridging position in the “Co-Mo-S” structure. Three different routes for the incorporation of Se can be given. The first is initial adsorption at the terminal Co position and subsequent spillover to the bridging position, displacing a sulfur atom (route B in scheme 4.2). A second possibility is the direct placement at a bridging position after the creation of a vacancy (route C). A different vacancy site and, thus, a dissimilar active site is created. The third route is a direct exchange of S with Se, kinetically possible at this high temperature (not shown in the scheme). Discrimination between these three routes could not be made, however, based on kinetic experiments [44], it was suggested that the second route (the creation of new active sites) is the most plausible one.

5. CONCLUSIONS AND OUTLOOK

The previous sections have described the application of *in-situ* EXAFS to catalytic systems in heterogeneous catalysis. Many aspects of performing an *in-situ* experiment are discussed; description of experimental set-up, *in-situ* cells and data-analysis schemes complement examples from the literature. *In-situ* EXAFS in catalysis is undisputed as a tool to determine the structure of a catalyst and, in some cases, the nature of the active site under well-defined conditions. The local order of an element in a catalyst can be determined under a wide range of conditions, for which unique *in-situ* cells have been designed. As the limitations of the conditions that can be applied during measurement can often be overcome, the full potential of *in-situ* XAS spectroscopy is not utilized. Thus, reports about new or improved *in-situ* cells have recently appeared and novel designs of *in-situ* cells are also expected. These new designs will allow measurement under experiment-specific and/or more extreme conditions. Continuous refinement of data-analysis procedures enables investigation of more complex systems. Aside from heterogeneous catalysis, homogeneous catalysis will greatly benefit from these improved data-analysis schemes. With an increasing amount of EXAFS studies on catalytic samples under real reaction conditions, where asymmetric distribution functions may play a role, data-analysis schemes that take this into account must be developed, and a theoretical basis must be developed and implemented into these codes. *In-situ* EXAFS will continue to be a source of structural information in catalytic research.

Even though EXAFS seems a quite-matured technique, new developments in data-analysis and instrumentation are reported. In addition, technical and theoretical developments open new possibilities to structural information of catalysts. Such techniques are Atomic XAFS [16], Diffraction Anom-

alous Fine Structure (DAFS) [45] and site-selective EXAFS [46]. AXAFS provides information about the electronic structure of the absorbing atom; DAFS gives chemical selective information by measuring the intensity of a diffraction reflection at energies below and above the absorption edge of an element; Site-selective EXAFS separates the EXAFS spectra of the various valences of one element.

In-situ spectroscopy is a highly developing field in science, and the combination of several *in-situ* spectroscopies will provide complementary information. Catalysts whose structures are very sensitive to the exact experimental conditions of a measurement need a synchronization of the spectroscopic techniques. Some examples of set-ups have already been reported and developments pose new challenges.

ACKNOWLEDGMENT

Rodney van der Mark is thanked for making Figure 15. Professor D. C. Koningsberger is thanked for his teaching of data analysis of EXAFS to JAvB, which is the basis of large parts of this paper.

REFERENCES

1. D. C. Koningsberger, and R. Prins, (eds) *X-ray Absorption: Principles, Applications, Techniques of EXAFS, SEXAFS and XANES* (John Wiley, New York, 1988)
2. Teo, B. K., EXAFS: Basic Principles and Data-analysis (Springer-Verlag, New York, 1986)
3. Nishihata, Y., Mizuki, J., Akoa, T., Tanaka, H., uenishi, M., Kimura, M., Okamoto, T., Hamada, N., *Nature*, 418, 164 (2002); Argo, A. M., Odzak, J. F., Lai, F. S., Gates, B. C., *Nature*, 415, 623 (2002).
4. Chapter Ressler this book
5. Chapter Knop this book
6. Koningsberger, D. C., Mojet, B. L., van Dorssen, G. E., Ramaker, D. E., *Topics in Catal.*, 10, 143 (2000).
7. (a) Bearden, J. A., Burr, A. F., *Rev. Mod. Phys.*, 39, 125 (1967); (b) Fuggle, J. C., M; N., anrtensson, *J. Electron Spectrosc. Relat. Phenom.*, 21, 275 (1980); (c) Cardona, M., Ley, L., Eds., *Photoemission in Solids I: General Principles* (Springer-Verlag, Berlin, 1978)
8. Chapter de Groot this book
9. Value of S0-square
10. Krause, M. O., *J. Phys. Chem. Ref. Data*, 8, 329 (1979).
11. (a) Ritchie, R. H., Ashley, J. C., *J. Phys. Chem. Solids*, 26, 1689 (1965); (b) Quinn, J. J., *Phys. Rev.*, 126, 1453 (1962); (c) Lacer, J., Garwin, E. L., *J. Appl. Phys.*, 40, 2766 (1969); (d) Veigle, W. J., *At. Data Tables*, 5, 51 (1951).
12. Stöhr, J., in *X-ray Absorption: Principles, Applications, Techniques of EXAFS, SEXAFS and XANES* (John Wiley, New York, 1988) D. C. Koningsberger, and R. Prins (eds)
13. Henke, B. L., Gullikson, E. M., Davis, J. C., *At. Data Nucl. Data Tables*, 54, 181 (1993).
14. http://ixs.iit.edu/catalog/XAFS_Programs
15. <http://www.xsi.nl/>
16. (a) Rehr, J. J., Booth, C. H., Bridges, F., Zabinsky, S. I., *Phys. Rev. B* 49, 12347 (1994); (b) Ramaker, D. E., Mojet, B. L., Koningsberger, D. C., O'Grady, W. E., *J. Phys. Condens. Matter*, 10, 8753 (1998); (c) Wende, H., Srivastava, Chauvistré, R., May, F., Baberschke, K., Arvanitis, D., Rehr, J. J., *J. Phys. Condens. Matter*, 9, L427 (1997).
17. van Dorssen, G. E., Ramaker, D. E., Koningsberger, D. C., Thesis Utrecht University (1999).
18. (a) Hu, T. D., Xie, Y. N., Jin, Y. L., Liu, T., *J. Phys: Condens Matter*, 9 (25) 5507; (b) Rehr, J. J., Booth, C. H., Bridges, F., *Phys. Rev. B*, 49 (17), 12347 (1994).
19. Sayers, D. E., Stern, E. A., Lytle, F. W., *Phys. Rev. Lett.*, 27, 1204 (1971).
20. (a) Martens, J. H. A., Prins, R., Koningsberger, D. C., *J. Phys. Chem.*, 93, 3179–3185 (1989); (b) van Zon, F. B. M. Maloney, S. D., Gates, B. C., Koningsberger, D. C., *J. Amer. Chem. Soc.*, 115, 10317–10326 (1993).
21. Gates, B. C., *Chem. Rev.*, 95, 511 (1995).
22. Tromp, M., van Bokhoven, J. A., Arink, A. M., Bitter, J. H., van Koten, G., Koningsberger, D. C., *Chem. Eur. J.* accepted
23. Koningsberger, D. C., in *Neutron and Synchrotron Radiation for Condensed Matter Studies, Vol. II*, eds. J. Baruchel, J. L. Hodeau, M. S. Lehman, J. R. Regnard, and C. Schlenker (Springer-Verlag, Berlin, 1994) p. 213
24. Bunker, B. A., Stern, E. A., *Phys. Rev. B*, 27, 1017 (1983).
25. (a) Ankudinov, A. L., Ravel, B., Rehr, J. J., Conradson, S. D., *Phys. Rev. B* 58, 7565 (1998); (b) Mustre de Leon, J., Rehr, J. J., Zabinski, S. I., Albers, R. C., *Phys. Rev. B*, 44, 4146 (1991).
26. Ressler, T., Wienold, J., Jentoft, R. E., Timpe, O., Neisius, T., *Solid State Commun.* 119, 169 (2001).
27. (a) Stern, E. A., *Phys. Rev. B*, 27, 9825 (1993); (b) Lee, P. A., Citrin, P. H., Eisenberger, P., Kincaid, B. M., *Rev. Mod. Phys.*, 53, 769 (1981).
28. Clausen, B. S., Nørskov, J. K., *Topics in Catal.*, 10, 221 (2000).
29. Lytle, F. W., Sayers, D. E., Stern, E. A., *Physica B*, 158, 701 (1988).
30. Bitter, J. H., Mojet, B. L., Janssen, M. D., Grove, D. M., van Koten, G., Koningsberger, D. C., *D. C. J. Synchrotron Rad.*, 6, 423 (1999).
31. (a) Persson, I., Penner-Hahn, J. E., Hodgson, K. O., *Inorg. Chem.*, 32, 2497 (1993); (b) Blackburn, N. J., Strange, R. W., Cruse, R. W., Karlin, K. D., *J. Am. Chem. Soc.*, 109, 1235 (1987); (c) Scott, R. A., Eidsness, M. K., *Comments Inorg. Chem.*, 7(5) 235 (1988); (d) Stemmler, T., Barnhart, T. M., Penner-Hahn, J. E., Tucker, C. E., Knochel, P., Böhme, H., Frenking, G., *J. Am. Chem. Soc.*, 117, 12489 (1995); (e) Henkel, G., Müller, A., Weissgräber, Buse, S., G., Soulimane, T., Steffens, G. C. M., Nolting, H-F., *Angew. Chem.*, 34, 1488 (1995); (f) Bertagnolli; H., Kaim, W., *Angew. Chem.*, 34, 771 (1995); (g) Huang, H., Liang, C. H., Penner-Hahn, J. E., *Angew. Chem.*, 37, 1264 (1998); (h) Barnhart, T. M., Penner-Hahn, J. E., *Physica B*, 208–209, 709 (1995).
32. (a) Clausen, B. S., Graback, K., Steffens, G., Hanssen, P. L., Topsøe, H., *Catal. Lett.*, 20, 23 (1993); (b) Nielsen, J. A., rubel, G., Clausen, B. S., *Nucl. Instrum. Methods B*, 97, 522 (1995); (c) Sankar, G., Thomas, J. M., Rey, F., Greaves, G. N., *Chem. Comm.*, 2549 (1995); (d) Sankar, G., Thomas, J. M., *Topics in Catal.*, 8, 1 (1999); (e) Hoffman, M. M., Darab, J. G., heald, S. T., Yonker, C. R., Fulton, J. L., *Chem. Geol.*, 167, 89 (2000).
33. (a) Caballero, A., González-Elipe, A. R., Fernández, A., Herrmann, J.-M., Dexpert, H., Villain, F., *J. Photochem. Photobiol. A: Chem.*, 78, 169 (1994); (b) San-Miguel, A., Itié, J. P., Polian, A., *Physica B*, 208–209, 506 (1995); (c) Sapelkin, A. V., Bayliss, S. C., Russell, D., Clark, S. M., Dent, A. J., *J. Synchrotron Rad.*, 7, 257 (2000); (d) Shen, G., Rivers, M. L., Wang, Y., Sutton, S. R., *Rev. Sci. Instrum.*, 72, 1273 (2001).
34. Murata, T., Nakagawa, K., Kimura, A., Otoda, N., Shimoyama, I., *Rev. Sci. Instrum.*, 66, 1437 (1995).
35. (a) Barlow, N., Brennan, C., Doyle, S. E., Greaves, G. N., Miller, M., Nahle, A. H., Roberts, K. J., Robinson, J., Sherwood, J. N., Walsh, F. C., *Rev. Sci. Instrum.*, 60, 2386 (1989); (b) Hansen, G. J., O'Grady, W. E., *Rev. Sci. Instrum.*, 61, 2127 (1990); (c) Herron, M. E., Doyle, S. E., Roberts, K. J., Robinson, J., Walsh, F. C., *Rev. Sci. Instrum.*, 63, 950 (1992); (d) Yoshitake, H., Yamazaki, O., Ota, K., *J. Electroanal. Chem.*, 287 (1994); (e) Haubold, H.-G., Wang, X. H., Jungbluth, H., Goerigk, G., Schilling, W., *J. Molec. Struct.*, 383, 283 (1996); (f) Antonio, M. R., Soderholm, L., Song, I., *J. Appl. Electrochem.*, 27, 784 (1997); (g) Nakai, I., Takahashi, K., Shiraishi, Y., Nakagome, T., Nishikawa, F., *J. Solid State Chem.* 140, 145 (1998).
36. Lytle, F. W., Wei, P. S. P., Greegor, R. B., Via, G. H., Sinfelt, J. H., *J. Chem. Phys.*, 70, 4849 (1979).
37. Kampers, F. W. H., Maas, T. M. J., van Grondelle, J., Brinkgreve, P., Koningsberger, D. C., *Rev. Sci. Instrum.*, 60, 2635 (1989).

38. (a) Jentoft, R. E., Deutsch, S. E., Gates, B. C., *Rev. Sci. Instrum.*, 67, 2111 (1996); (b) Meitzner, Bare, S. R., Parker, D., Woo, H., Fischer, D. A., *Rev. Sci. Instrum.*, 69, 2618 (1998).
39. Odzak, J. F., Argo, A. M., Lai, F. S., Gates, B. C., Pandya, K., Feraria, L., *Rev. Sci. Instrum.*, 72, 3943 (2001).
40. (a) Shannon, I. J., Maschmeyer, T., Sankar, G., Thomas, J. M., Oldroyd, R. D., Sheehy, M., Madill, D., Waller, A. W., Townsend, R. P., *Cat. Lett.*, 44, 23 (1997); (b) Kappen, P., Grunwald, J.-D., Hammershøi, B. S., Tröger, L., Clausen, B. S., *J. Catal.*, 198, 56 (2001).
41. Moggridge, G. D., Schroeder, S. L. M., Lambert, R. M., Rayment, T., *Nucl. Instr. And Meth. In Phys. Res. B*, 97, 28 (1995).
42. Grunwaldt, J.-D.- Basini, L., Clausen, B. S., *J. Catal.*, 200, 321 (2001).
43. Leliveld, B. R. G., van Dillen, J. A. J., Geus, J. W., Koningsberger, D. C., de Boer, M., *J. Phys. Chem. B*, 101, 11160 (1997).
44. Leliveld, B. R. G., van Dillen, J. A. J., Geus, J. W., Koningsberger, D. C., *J. Catal.*, 175, 108 (1998).
45. DAFS
46. site selective XAFS